Pressure and oxygen-isotope substitution on density-wave transitions in $La_4Ni_3O_{10}$

Rustem Khasanov,[1,*] Vahid Sazgari,[1] Thomas J. Hicken,[1] Igor Plokhikh,[1,2] Marisa Medarde,[1] Ekaterina Pomjakushina,[1] Lukas Keller,[1] Vladimir Pomjakushin,[1] Marek Bartkowiak,[1] Szymon Królak,[3,4] Michał J. Winiarski,[3,4] Alexander Steppke,[1] Jonas A. Krieger,[1] Hubertus Luetkens,[1] Tomasz Klimczuk,[3,4] Christof W. Schneider,[1] Dariusz J. Gawryluk,[1] and Zurab Guguchia[1]

[1]*PSI Center for Neutron and Muon Sciences CNM, 5232 Villigen PSI, Switzerland*

[2]*Department of Physics, TU Dortmund University, Dortmund 44227, Germany*

[3]*Faculty of Applied Physics and Mathematics, Gdańsk University of Technology, Narutowicza 11/12, Gdansk 80-233, Poland*

[4]*Advanced Materials Center, Gdańsk University of Technology, Narutowicza 11/12, Gdansk 80-233, Poland*

(Received 6 May 2025; accepted 19 January 2026; published 9 March 2026)

Understanding the interplay between magnetism and superconductivity in nickelate systems is a key objective in condensed matter physics. Gaining microscopic insights into magnetism—particularly as it emerges near superconductivity—requires a synergistic approach that combines complementary experimental techniques with controlled tuning of external parameters. In this paper, we present a systematic investigation of the three-layer Ruddlesden-Popper (RP) nickelate $La_4Ni_3O_{10}$ using muon-spin rotation/relaxation (μSR) and resistivity measurements. At ambient pressure, two incommensurate spin-density-wave (SDW) transitions are identified at $T_{SDW} \simeq 132$ K and $T^* \simeq 80$–90 K. Comparison of the observed internal magnetic fields with dipole-field calculations reveals a magnetic structure consistent with antiferromagnetically coupled SDW order on the outer two Ni-O layers, with smaller moments on the inner Ni-O layer. Above T^*, the moments lie primarily in the *ab* plane, but below this temperature they undergo a subtle distortion and develop a *c*-axis component. The internal fields at the muon stopping sites appear abruptly at T_{SDW}, suggesting a first-order-like nature of the SDW transition, which is closely linked to the charge-density wave (CDW) order occurring at the same temperature ($T_{SDW} = T_{CDW}$). Under applied pressure, all transition temperatures—including T_{SDW}, T^*, and T_{CDW}—are suppressed at a nearly uniform rate of $\simeq -13$ K/GPa. This behavior contrasts with that of the two-layer RP nickelate $La_3Ni_2O_7$, where pressure enhances the separation between the SDW and CDW transitions. The oxygen-isotope substitution ($^{16}O \rightarrow {}^{18}O$) reveals that the CDW transition temperature shifts to higher values in the ^{18}O-substituted samples. The isotope effect on T_{SDW} and T^* differs significantly. Specifically, when the CDW and SDW orders are intertwined, a notable isotope effect is observed on T_{SDW}, leading to equal transition temperatures and nearly identical isotope shifts for both T_{CDW} and T_{SDW}. In contrast, at T^*, where the SDW transition occurs independently of the CDW, no isotope effect is detected.

DOI: 10.1103/nrqn-m22c

I. INTRODUCTION

The exploration of nickelates, including those belonging to the Ruddlesden-Popper (RP) series $La_{(n+1)-x}Pr_xNi_nO_{3n+1}$ ($n = 2, 3$), has garnered significant attention in condensed matter physics and materials science due to their intriguing structural, electronic, and magnetic properties [1–23]. The recent observation of high-temperature superconductivity under high pressure in a member of the RP series with $n = 2$, has further enhanced interest in this class of materials, highlighting their potential for groundbreaking discoveries. Relevant studies include recent works on $La_{3-x}Pr_xNi_2O_7$ under high pressure, which demonstrate its superconducting properties [1,5,14], as well as investigations into the electronic and structural properties of $La_{4-x}Pr_xNi_3O_{10}$ [2,8,14,17–20]. Among these, the compound $La_4Ni_3O_{10}$, a member of the RP series with $n = 3$, stands out due to its proximity to potential metal-to-metal transitions [10–12,21,22], charge ordering [2,8], and unconventional superconductivity [3,4,7]. Such features make it a promising candidate for understanding correlated electron systems and for exploring phenomena under extreme conditions.

At ambient pressure, $La_4Ni_3O_{10}$ exhibits two types of order: charge density wave (CDW) and spin density wave (SDW) states. These states have similar ordering temperatures and are strongly intertwined, highlighting the complex interplay between charge and spin degrees of freedom in this material [2]. The phase diagram of $La_4Ni_3O_{10}$ reveals a delicate balance between the density wave (DW) states and the superconducting phase, with pressure acting as a key tuning parameter [3,4,7]. As pressure increases, the suppression of DW order appears to coincide with the emergence of superconductivity, indicative of a strong interplay between these competing phases. However, the exact nature of the DW

*Contact author: rustem.khasanov@psi.ch

state suppressed by external pressure remains unidentified. For comparison, in the double-layer RP nickelate $La_3Ni_2O_7$, the SDW and CDW ordering temperatures (T_{SDW} and T_{CDW}) exhibit opposite trends: T_{SDW}, as defined by μSR experiments, increases with pressure, while T_{CDW}, determined from resistivity measurements, decreases [13].

Beyond pressure, isotope substitution was shown to influence the CDW and SDW transition temperatures in various materials [24–33]. The formation of charge- and spin-density waves arises due to collective electronic instabilities, often accompanied by lattice distortions, making these phases highly sensitive to phononic contributions. Variations in the transition temperatures (T_{CDW} and T_{SDW}) upon isotope substitution provide insight into the relative importance of electron-phonon interactions versus purely electronic effects in stabilizing these ordered states.

This paper presents a systematic investigation of $La_4Ni_3O_{10}$ using a combination of muon-spin rotation/relaxation (μSR) and resistivity measurements. These complementary techniques provide detailed insights into the magnetic and electronic behavior of the material under various conditions—particularly at ambient and high pressures, as well as upon substitution of ^{16}O with the ^{18}O isotope. The main findings are summarized as follows:

(1) At ambient pressure, $La_4Ni_3O_{10}$ exhibits two SDW transitions at $T_{SDW} \simeq 132$ K and $T^* \simeq 80$–90 K, with magnetic moments preferentially aligned within the *ab* planes. Comparison of the observed internal magnetic fields with dipolar-field calculations reveals a magnetic structure consistent with antiferromagnetically coupled SDW order on the outer two Ni-O layers and smaller Ni moments on the inner Ni-O layer. The transition at T^* is further associated with a subtle reorientation of Ni moments, acquiring a *c*-axis component at lower temperatures.

(2) Under applied pressure, all transition temperatures—T_{SDW}, T^*, and T_{CDW}—are suppressed. Despite this, the SDW and CDW transitions remain closely linked and are most likely strongly intertwined. This behavior contrasts with that of the two-layer RP nickelate $La_3Ni_2O_7$, where pressure induces an increasing separation between the two density-wave orders [13].

(3) Oxygen-isotope effect (OIE) experiments reveal that when the CDW and SDW transitions are intertwined ($T_{CDW} \simeq T_{SDW}$), the ordering temperatures shift to higher values in the ^{18}O-substituted sample. The isotope shifts are found to be comparable for both transitions, with $^{18}T_{CDW} - {}^{16}T_{CDW} \simeq {}^{18}T_{SDW} - {}^{16}T_{SDW} \simeq 2.1$ K. In contrast, the OIE on the spin-reorientation transition at T^*—where the SDW state evolves independently from the CDW—is negligible.

Our results underscore the intertwined nature of SDW and CDW order in $La_4Ni_3O_{10}$, consistent with behavior observed in other correlated systems such as the cuprates [34–40] and hole-doped nickelates [41–43]. Given the distinct pressure-dependent evolution of SDW order observed in $La_3Ni_2O_7$ (Ref. [13]) and $La_4Ni_3O_{10}$ (this work), we propose that—if the behavior of the density-wave transitions persists at higher pressures—the pressure-induced suppression of CDW order may be a possible mechanism driving the emergence of high-temperature superconductivity in Ruddlesden-Popper nickelates. Notably, while T_{CDW} decreases with pressure in both systems, T_{SDW} evolves differently: it increases in $La_3Ni_2O_7$ but decreases in $La_4Ni_3O_{10}$, underscoring fundamental differences in their electronic phase behavior.

TABLE I. Results of characterization of $La_4Ni_3O_{10}$ samples by means of x-ray diffraction and thermogravimetry.

	$La_4Ni_3O_{10-\delta}$	$La_4Ni_3\ ^{16}O_{10-\delta}$	$La_4Ni_3\ ^{18}O_{10-\delta}$
Symmetry Group	*Bmab*	*Bmab*	*Bmab*
a (Å)	5.4140(3)	5.4163(3)	5.4134(3)
b (Å)	5.4622(2)	5.4623(3)	5.4602(2)
c (Å)	27.9766(1)	27.9710(1)	27.9715(3)
Oxygen content	9.99(1)	10.04(1)	10.07(2)

The paper is organized as follows. Sec. II describes the characterization of $La_4Ni_3O_{10-\delta}$ samples using x-ray diffraction, thermogravimetry, neutron powder diffraction, Raman, and resistivity measurements. Section III presents zero-field μSR measurements on the pristine $La_4Ni_3O_{10-\delta}$ sample, along with results of muon stopping site and dipolar-field calculations. Experiments conducted under hydrostatic pressure conditions are detailed in Sec. IV. Section V presents Raman, μSR, and resistivity studies of $^{16}O/^{18}O$ isotope-substituted samples. The conclusions follow in Sec. VI.

II. SAMPLE CHARACTERIZATION

The initially grown $La_4Ni_3O_{10-\delta}$ sample was divided into three parts. The first part, hereafter referred to as the "pristine" sample, was used for ambient- and high-pressure experiments. The remaining two parts were used to prepare oxygen-isotope-substituted samples ($La_4Ni_3\ ^{16}O_{10}$ and $La_4Ni_3\ ^{18}O_{10}$) by annealing them in either a $^{16}O_2$ or $^{18}O_2$ atmosphere.

Figures 1(a) and 1(b) show the x-ray diffraction patterns collected at room temperature. Le Bail refinement of the x-ray data for the pristine sample yields a monoclinic structure ($P2_1/a$, space group No. 14), with lattice parameters $a = 5.4162(3)$ Å, $b = 5.4642(2)$ Å, $c = 27.984(1)$ Å, and $\beta = 90.256(4)^\circ$, in agreement with previous reports [2–4,7,23]. To reduce the number of refined parameters for the oxygen-isotope-substituted samples—and noting that the monoclinic $P2_1/a$ symmetry group with $\beta \simeq 90^\circ$ is only marginally distorted from the orthorhombic *Bmab* space group—the x-ray data for all $La_4Ni_3O_{10-\delta}$ samples were further refined using the *Bmab* symmetry group. The results of the x-ray refinements are summarized in Table I. All samples exhibit nearly identical lattice constants.

The oxygen content $(10 - \delta)$ was determined using thermogravimetric analysis, as shown in Figs. 1(c) and 1(d). A small amount of material (≃20–40 mg) was heated from room temperature to 1000 °C at a rate of 1 °C/min in a flowing H_2/He gas mixture (5 vol.% hydrogen and 95 vol.% helium). The total weight loss was attributed to the reduction of fully oxidized samples to metallic nickel and La_2O_3. Two important points need to be mentioned:

(1) The weight loss in the ^{18}O-substituted samples was bigger than that in the pristine and ^{16}O-substituted ones due to the heavier mass of ^{18}O atoms compared to ^{16}O.

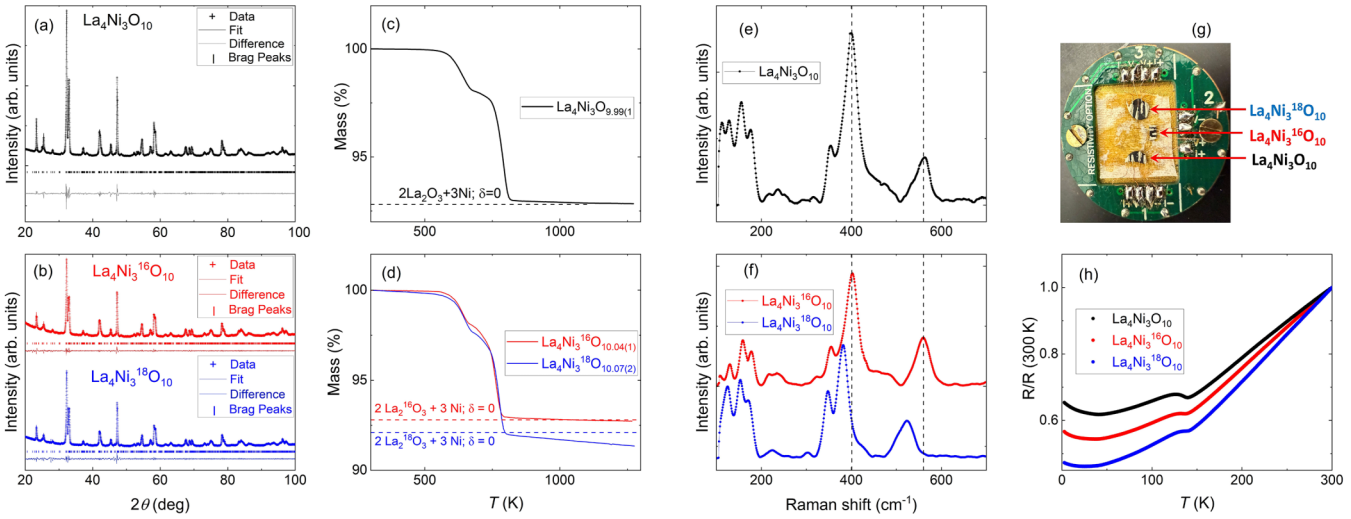

FIG. 1. X-ray diffraction patterns of pristine [panel (a)] and oxygen-isotope ($^{16}O/^{18}O$) substituted [panel (b)] $La_4Ni_3O_{10}$ samples taken at room temperature. The x-ray data were refined using the $P2_1/a$ [panel (a)] and *Bmab* [panel (b)] space groups. Thermogravimetric curves of the pristine [panel (c)] and oxygen-isotope substituted [panel (d)] $La_4Ni_3O_{10}$ samples. Room-temperature Raman spectra collected for pristine [panel (e)] and oxygen-isotope-substituted [panel (f)] $La_4Ni_3O_{10}$ samples. The dashed lines indicate several Raman modes of the samples containing the lighter oxygen isotope. (g) Photograph of polycrystalline $La_4Ni_3O_{10}$, $La_4Ni_3\ ^{16}O_{10}$, and $La_4Ni_3\ ^{18}O_{10}$ samples mounted on the measurement chip and prepared for resistivity measurements. (h) Temperature dependence of resistivity normalized to its 300 K value $R(T)/R(300)$ for pristine and isotope-substituted $La_4Ni_3O_{10}$ samples.

(2) Above $T \sim 750$ K, the decomposed ^{18}O-substituted sample continue to lose weight, whereas the weight remains nearly constant for the pristine and ^{16}O-substituted ones. This behavior may be attributed to the partial exchange of ^{18}O atoms in La_2O_3 with residual ^{16}O causing back exchange.

The results of the thermogravimetric analysis are summarized in Table I. Considering the second point above, the $La_4Ni_3O_{10-\delta}$ samples studied here can be considered nearly oxygen stoichiometric.

The room temperature Raman experiments confirm the appearance of several lines in the region ranging from 100 up 700 cm^{-1} in agreement with the results of Refs. [44–47]. The Raman lines stay nearly at the same positions at pristine and ^{16}O-substituted samples, while they are clearly shifted to the lower frequencies in ^{18}O-substituted ones [see Figs. 1(e) and 1(f)]. In order to ensure on the uniform distribution of oxygen isotopes, several experiments at different laser-beam positions were performed.

The resistivity measurements were performed simultaneously on the three samples, all mounted on the same measurement chip [see Fig. 1(g)]. The resulting resistivity [$R(T)$] curves are shown in Fig. 1(h). The $R(T)$ dependencies exhibit a weak anomaly near $T \simeq 130$ K, which is attributed in the literature to the onset of intertwined SDW and CDW orders [2,3].

High-resolution neutron powder diffraction (NPD) data were collected at $T = 1.7$, 100, and 150 K using the HRPT diffractometer. The results indicate the absence of a structural phase transition within this temperature range. The refined crystal structure is consistent with the $P2_1/a$ space group previously determined from x-ray diffraction [48]. The temperature evolution of the incommensurate SDW magnetic peak at $(0, 0.574, 2)$ was monitored by collecting high-intensity NPD patterns using the DMC diffractometer. The results of the neutron powder diffraction studies on pristine $La_4Ni_3O_{10}$ samples are presented in the Supplemental Material [49].

III. AMBIENT-PRESSURE STUDIES OF PRISTINE $La_4Ni_3O_{10-\delta}$

A. Zero-field μSR

The zero-field (ZF) μSR response of $La_4Ni_3O_{10}$ measured at temperatures $T = 5$ and 110 K is presented in Figs. 2(a)–2(d). Figures 2(a) and 2(b) display the ZF asymmetry spectra, which represent the time evolution of the muon-spin polarization, while Figs. 2(c) and 2(d) show the Fourier transform of the data, illustrating the distribution of internal fields. Evidently, the time spectra and magnetic field distributions differ significantly between high and low temperatures. The number of peaks in the field distribution changes from five at $T = 5$ K [Fig. 2(c)] to two at $T = 110$ K [Fig. 2(d)]. The evolution of the magnetic field distribution is better visualized in the waterfall graph [Fig. 2(e)], which shows that the five-peak structure transitions to a two-peak one at temperatures around 90 K.

Analysis revealed that the ZF-μSR time spectra cannot be fitted using simple cosine-type oscillating functions, which are typically used to describe a commensurate magnetic order [13,50–52]. Instead, the magnetic field distributions shown in Figs. 2(c) and 2(d) suggest the presence of long tails extending from the peak positions to approximately zero field. This feature is characteristic of incommensurate magnetic order, which is typically described by an Overhauser-type distribution within the field domain and by a zeroth-order Bessel function (J_0) within time domain [53–56].

The fit of the ZF-μSR data was performed using Eq. (A1). The magnetic (m) and nonmagnetic (nm) components, with

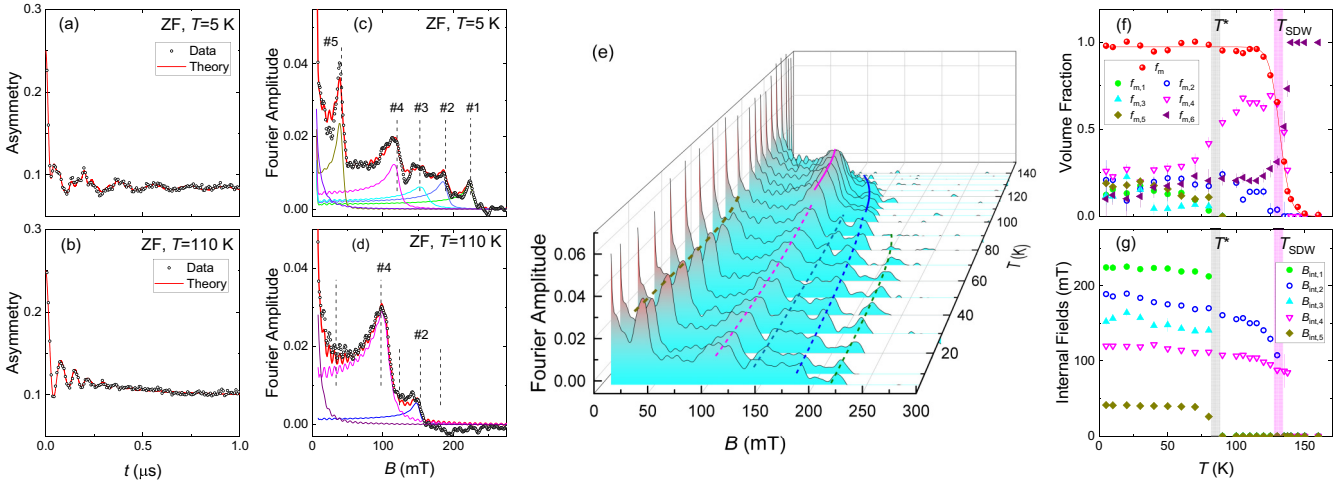

FIG. 2. Zero-field μSR time spectra of the pristine $La_4Ni_3O_{10}$ sample collected at $T = 5\,\mathrm{K}$ [panel (a)] and $T = 110\,\mathrm{K}$ [panel (b)]. (c)–(d) Fourier transforms of the data shown in panels (a) and (b). Solid lines represent the fit (red) and individual fit components. Dashed lines indicate the positions of internal field peaks expected from the six-component fits. (e) Temperature evolution of the Fourier transform spectra, showing the transition of the magnetic field distribution from a five-peak to a two-peak structure. (f) Temperature dependence of the ZF-μSR signal fractions. The solid line corresponds to a fit of Eq. (1) to $f_\mathrm{m}(T)$. (g) Temperature dependencies of the internal fields. The gray and pink lines in panels (f) and (g) indicate the positions of the magnetic ordering temperatures T^* and T_SDW, respectively.

corresponding weights f_m and $1 - f_\mathrm{m}$, were described using Eqs. (A2) and (A3), respectively. The magnetic term [Eq. (A2)] required the presence of six components (five oscillating and one fast relaxing) for the low-temperature data ($T \lesssim 90\,\mathrm{K}$), and three components (two oscillating and one fast relaxing) for the high-temperature data ($T \gtrsim 90\,\mathrm{K}$).

The temperature evolution of magnetic volume fractions ($f_{\mathrm{m},1}$ to $f_{\mathrm{m},6}$) is shown in Fig. 2(f). The total magnetic fraction f_m represents the sum of individual $f_{\mathrm{m},i}$ components ($f_\mathrm{m} = \sum f_{\mathrm{m},i}$). The solid line corresponds to the fit by means of the phenomenological expression [24]:

$$f_\mathrm{m}(T) = f_\mathrm{m}(0)\left[1 + \exp\left(\frac{T - T_\mathrm{SDW}}{\Delta T_\mathrm{SDW}}\right)\right]^{-1}, \qquad (1)$$

where $f_\mathrm{m}(0)$ and ΔT_SDW represent the zero-temperature value of the magnetic fraction and the width of the SDW transition, respectively. The fit yields $f_\mathrm{m}(0) = 0.98(1)$, $T_\mathrm{SDW} = 131.8(4)\,\mathrm{K}$, and $\Delta T_\mathrm{SDW} = 3.8(3)\,\mathrm{K}$. Consequently, below the SDW transition, nearly 100% of the sample response is attributed to the magnetic contribution. The sharpness of the magnetic transition [$\Delta T_\mathrm{SDW} = 3.8(3)\,\mathrm{K}$] suggests that magnetism in $La_4Ni_3O_{10}$ sets in homogeneously.

The temperature dependence of the internal magnetic fields ($B_{\mathrm{int},1}$ to $B_{\mathrm{int},5}$) is shown in Fig. 2(g). Two transitions, corresponding to changes in the internal fields at $T^* \simeq 80$–$90\,\mathrm{K}$ and $T_\mathrm{SDW} \simeq 132\,\mathrm{K}$, are clearly observed. The first transition, at $T \simeq T_\mathrm{SDW}$, is characterized by the abrupt appearance of internal fields around $B_\mathrm{int} \sim 100\,\mathrm{mT}$. This behavior indicates that the magnetic transition at $T_\mathrm{SDW} \simeq 132\,\mathrm{K}$ is first-order-like and is likely driven by a different kind of ordering, such as a structural transition (as observed in CrAs [57,58]) or a nematic transition (as seen in Fe-based superconductors [59]). In $La_4Ni_3O_{10}$, the spin-density-wave and charge-density-wave transitions occur simultaneously, as reported in Ref. [2]. This suggests that the CDW transition may be the primary one, with charge modulation triggering the onset of SDW order. It is worth noting that the change in the ordered volume fraction around T_SDW, as measured by μSR and indicative of a first-order transition, would not be captured by neutron diffraction, which averages over the entire sample volume. As a result, the magnetic transition may appear smooth and second-order-like in neutron measurements (see, e.g., Fig. 1(e) in Ref. [2]).

The second magnetic transition at $T^* \simeq 80$–$90\,\mathrm{K}$ is characterized by a change in the magnetic field distribution from a two-peak to a five-peak structure. Note that the magnetic transitions at T_SDW and T^* can be identified using different sets of fitting parameters. T_SDW is best determined from the temperature evolution of the magnetic volume fraction f_m [Fig. 2(f)]. In contrast, $B_{\mathrm{int},i}(T)$ [Fig. 2(g)] does not approach zero due to the first-order nature of the magnetic transition. Conversely, T^* is not reflected in the volume fraction dependencies but is associated with the loss of three out of five internal field components for temperatures exceeding 90 K. Both magnetic transitions are represented by the pink and gray vertical lines in Figs. 2(f) and 2(g). A more systematic studies of the transition at T^* were performed for the isotope-substituted samples, which are presented in Sec. V.

B. Muon stopping sites and dipolar-field calculations

To understand the μSR data collected at ambient pressure, muon stopping site calculations were performed. Three distinct sites, listed in Table II, were identified. Although these sites span a range of energies, all are likely to be occupied and show negligible displacement of the surrounding lattice, suggesting that the muon acts as a faithful probe of the system. Each site is located in a different layer of the material, near the Ni-O trilayer structure, as illustrated in Fig. 3(a). All three muon sites lie between 0.8 and 1 Å from the nearest O atom, as is often found. The lowest-energy site is located in the La plane, the highest-energy site in the plane containing the

TABLE II. The three identified muon stopping sites in $La_4Ni_3O_{10}$. The energies are given with respect to the lowest-energy calculation. Fractional coordinates are given in terms of the conventional unit cell.

Muon site	Energy (eV)	Coordinates
I	0	(0.396, 0.904, 0.940)
II	0.18	(0.204, 0.790, 0.530)
III	0.22	(0.390, 0.696, 0.999)

inner Ni-O layer, and the intermediate-energy site lies in a plane between the other two. The dipole field at the muon stopping site were calculated by assuming all three muon sites are equally occupied. Note that very similar field distributions are produced by just considering the two lower-energy muon sites; therefore, one cannot be certain whether or not the third site is occupied. It was further assumed that there is no contribution to the spectra from the contact hyperfine interaction that would arise from overlap between the electronic and muon-spin wavefunctions; this is consistent with our work on $La_3Ni_2O_7$ [13]. As the magnetic structure is not fully understood, we have taken the structure proposed in Ref. [2] as a starting point, with an antiferromagnetically coupled spin-density wave on the outer two Ni-O layers, using the q vector $\mathbf{q} = (0, 0.574, 0)$ obtained in our NPD measurements (see the Supplemental Material [49]). Note that this value of the q vector stays relatively close to $\mathbf{q} = (0, 0.62, 0)$ reported by Zhang *et al.* [2]. Whilst this reproduces many of the features seen in the experiment, we find that this structure gives too much weight to fields near zero; to resolve this, we introduce a small Ni moment on the inner Ni-O layer. As μSR is not a q resolved probe, we cannot categorically determine the ordering in this layer, hence we make the simplest assumption that the inner layer is also an SDW with the same wave vector, with a phase offset of 90° from both outer layers [as shown in Fig. 3(b)]. We use a maximum Ni moment of $2.81\mu_B$ on the outer Ni-O layers, consistent with the full moment of Ni, and the inner moment scaled to ∼8% of this value, as predicted by density-functional theory (DFT) calculations [60].

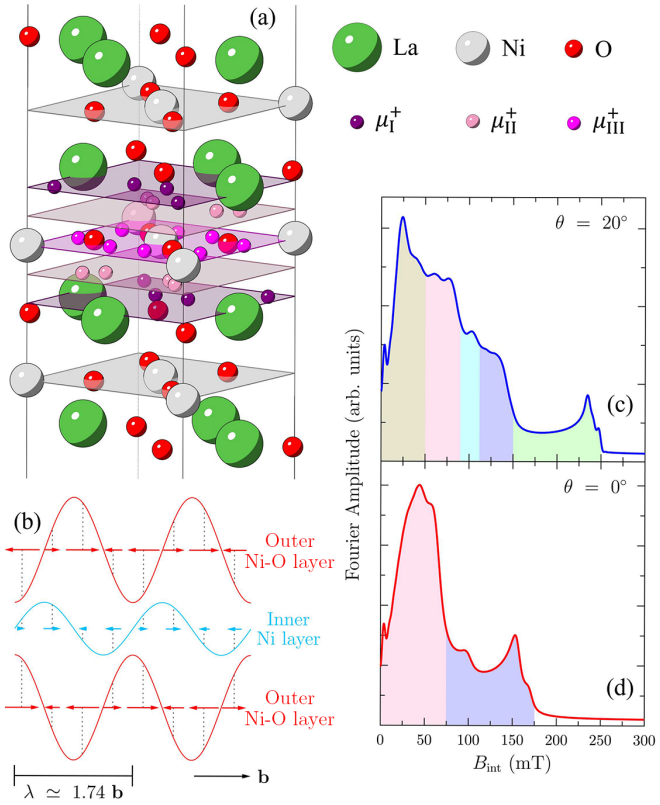

FIG. 3. (a) The three muon stopping sites with their relation to the Ni-O trilayer structure. Symmetrically equivalent positions are all shown, although in the experiment only one position is occupied at any one time. (b) The magnetic structure used in simulations of the ZF-μSR spectra. There is a large Ni moment on the outer Ni-O layers, with a small one on the inner Ni-O layer. All moments point in the ***b*** direction, and form an SDW. There is a phase shift of 90° between each layer. (c), (d) Simulations of the dipole field at the muon stopping sites with the moments either pointing in the *ab* plane ($\theta = 0°$), or rotated toward the c axis ($\theta = 20°$). Colors under the curves correspond to the colors of the different fit components in Figs. 2(c) and 2(d), highlighting the qualitative similarity.

Considering first the situation where the moments point in the b direction, as predicted in Ref. [2], our simulations qualitatively resemble the experimental data above 90 K [as shown in Fig. 3(d)]. The majority of muons experience a low internal field, with the remainder contributing to a continuous distribution, peaking maximally around 150 mT. This suggests that at high T, the magnetic structure is that of coupled SDWs, with the magnetic moments pointing in the *ab* plane, and a smaller moment on the inner Ni-O layer. At low T, the spectra exhibit additional peaks, suggesting the field at the muon site becomes more varied. There are myriad ways to break this degeneracy; we have considered two key scenarios. (1) Increasing Ni moment on the inner Ni-O layer. This leads to many more peaks in the spectra, but leaves very little weight at lower magnetic fields, and therefore seems inconsistent with the experimental data. (2) Canting the moments out of the *ab* plane. There are many ways that this could occur, so we have considered the simplest case of rotating all the moments in the same way. We show in Fig. 3(c) the result when all the moments are rotated $\theta = 20°$ toward the c axis. This produces a qualitatively good match with the experimental data [Figs. 2(c) and 2(d)], with the key features all reproduced with approximately the correct weighting. As for $\theta = 0°$, the absolute magnitude of the internal field is not correct at lower fields, suggesting that, whilst the main features of the magnetic structure are well explained, there are some subtle details that a q-resolved probe will be best placed to explore. Our two key results are that (1) there is likely a small magnetic moment on the inner Ni-O layers and (2) that it is most likely that the moments lie in the *ab* plane above 90 K, before subtly distorting, gaining a c-axis component at lower T.

IV. EXPERIMENTS UNDER HYDROSTATIC PRESSURE

A. μSR experiments

In μSR experiments conducted under pressure, a significant fraction of muons (approximately 50%) stop in the pressure cell walls, contributing to the μSR response as

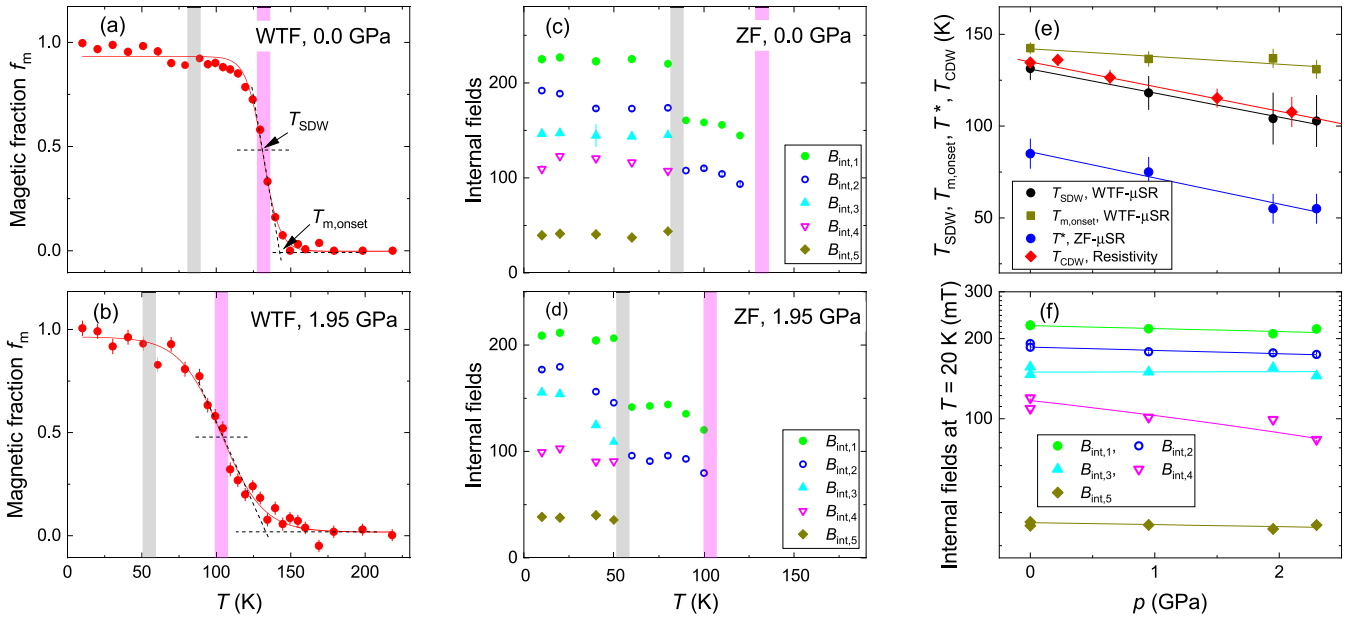

FIG. 4. Temperature dependence of the magnetic volume fraction f_m measured in WTF-μSR experiments at $p = 0.0$ GPa [panel (a)] and $p = 1.95$ GPa [panel (b)]. The solid lines represent fits of Eq. (1) to the data. Temperature evolution of the internal fields measured in ZF-μSR experiments at $p = 0.0$ GPa [panel (c)] and $p = 1.95$ GPa [panel (d)]. The gray and pink lines in panels (a)–(d) indicate the positions of the magnetic ordering temperatures T^* and T_{SDW}, respectively. (e) Pressure dependence of the magnetic ordering temperatures $T_{m,onset}$, T_{SDW}, and T^*, as well as the charge-density-wave ordering temperature T_{CDW}. The solid lines are linear fits. (f) Pressure dependence of the internal field components measured in ZF-μSR experiments at $T = 20$ K. The solid lines are linear fits.

background. Fitting the μSR data under pressure using Eq. (A1) requires knowledge of the background contribution from the pressure cell, which was determined in a separate set of experiments [61]. The analysis of ZF-μSR under pressure data was performed using Eqs. (A1)–(A3). The μSR experiments conducted in a weak transverse field (WTF, $B_{WTF} = 5$ mT), i.e., with a field applied perpendicular to the initial muon-spin polarization, were analyzed using Eq. (A1), with the sample part described by Eq. (A4).

The temperature dependence of the magnetic volume fraction, obtained from WTF experiments at $p = 0.0$ and 1.95 GPa, are shown in Figs. 4(a) and 4(b). Solid lines represent fits of Eq. (1) to the $f_m(T)$ data. The onset of the magnetic ordering ($T_{m,onset}$) is determined as the crossing point of the linearly extrapolated $f_m(T)$ line in the vicinity of the magnetic transition with $f_m = 0$ line. Temperature dependencies of internal fields, derived from fits to ZF-μSR data, are shown in Figs. 4(c) and 4(d). The magnetic ordering temperatures T^* and T_{SDW} are indicated by gray and pink vertical lines.

The pressure dependencies of T_{SDW} and $T_{m,onset}$, as determined from WTF-μSR data and T^*, obtained from changes in the magnetic field distribution—specifically, the transition from a five-peak to a two-peak structure in ZF-μSR data—are presented in Fig. 4(e). The solid lines represent linear fits:

$$T_{m,onset}(p) = 142.1(1.5) - p \times 4.2(1.2)\ \text{K/GPa},$$
$$T_{SDW}(p) = 131.1(8) - p \times 13.1(7)\ \text{K/GPa},$$
$$T^*(p) = 86(3) - p \times 14(2)\ \text{K/GPa}.$$

The nearly identical pressure derivatives of $\simeq -13$ K/GPa for $T_{SDW}(p)$ and $T^*(p)$ indicate that these transition temperatures decrease at a similar rate with increasing pressure. In contrast, $T_{m,onset}$ decreases approximately three times more slowly.

The pressure-enhanced difference between $T_{m,onset}$ and T_{SDW} suggests that magnetic fluctuations—acting as precursors to static magnetic order and detectable by μSR—are effectively enhanced under pressure. Indeed, the separation between $T_{m,onset}$ and T_{SDW} increases from approximately 10 K at $p = 0.0$ GPa to about 30 K at $p \simeq 2.3$ GPa.

The pressure dependence of internal fields ($B_{int,1}$ to $B_{int,5}$) measured at $T = 20$ K is shown in Fig. 4(f). Typically, the internal field at the muon stopping site is proportional to the value of the ordered magnetic moments, i.e., to the magnetic moments of Ni ions in our case. However, in $La_4Ni_3O_{10}$, the situation appears more complex. Linear fits of $B_{int,i}(p)$s reveal that three internal fields ($B_{int,1}$, $B_{int,2}$, and $B_{int,5}$) decrease with pressure at a similar rate, $\mathrm{d}\ln B_{int,i}/\mathrm{d}p \simeq -0.018(5)\ \text{GPa}^{-1}$. In contrast, $B_{int,3}$ remains nearly constant [$\mathrm{d}\ln B_{int,3}/\mathrm{d}p = 0.003(10)\ \text{GPa}^{-1}$], while $B_{int,4}$ decreases six times faster [$\mathrm{d}\ln B_{int,4}/\mathrm{d}p = -0.128(10)\text{GPa}^{-1}$]. This suggests that pressure not only reduces the value of ordered magnetic moments, which would result in a similar pressure evolution for all internal fields, but may also lead to slight rearrangements of magnetic moments, causing different pressure dependencies for $B_{int,3}$ and $B_{int,4}$. Further studies, particularly precise determinations of the magnetic structure at various pressures, are needed to explain this observation.

B. Resistivity measurements

The results of resistivity measurements at pressures ranging from 0.22 to 2.1 GPa are presented in Fig. 5. The anomaly in the $R(T)$ data, which is associated in the literature with

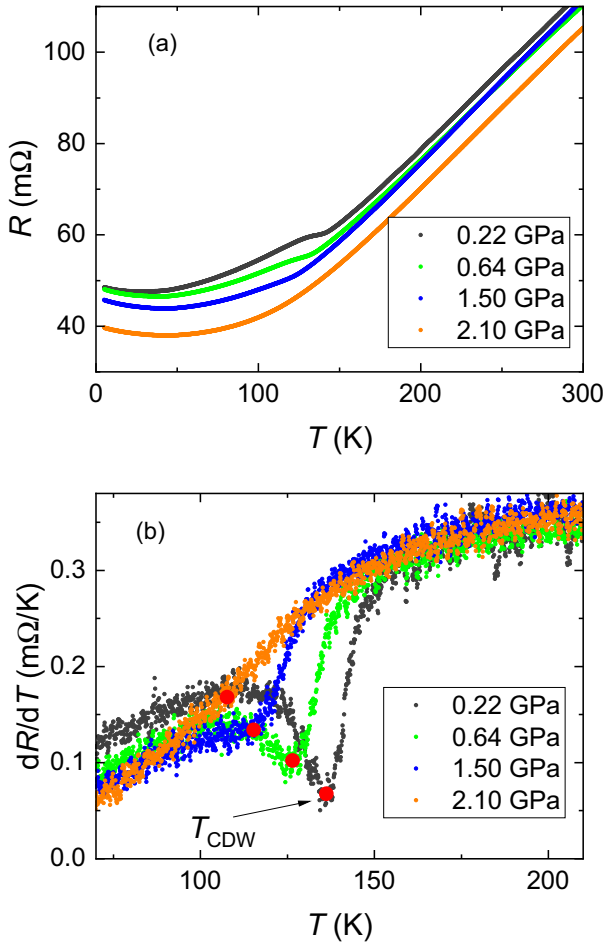

FIG. 5. (a) Temperature dependencies of resistivity R measured at pressures $p = 0.22$, 0.64, 1.50, and 2.10 GPa. (b) First derivatives of the resistivity curves. Red dots indicate the CDW transition temperature T_{CDW}.

the appearance of the CDW ordered state, is visible at low pressures but nearly vanishes at $p \simeq 2.1$ GPa [Fig. 5(a)]. The data suggest that pressure suppresses both the onset of CDW transition and the associated anomaly in $R(T)$ curves. To make CDW feature more apparent, Fig. 5(b) shows the first derivatives of the $R(T)$ data. The "dip" in $\mathrm{d}R(T)/\mathrm{d}T$ curves was associated with the CDW transition, and it is marked by red points in Fig. 5(b).

The pressure dependence of T_{CDW}, combined with $T_{\mathrm{m,onset}}$, $T_{\mathrm{SDW}}(p)$, and $T^*(p)$, is shown in Fig. 4(e). A linear fit yields

$$T_{\mathrm{CDW}}(p) = 135.1(8)\,\mathrm{K} - p \times 13(2)\,\mathrm{K/GPa},$$

in agreement with the $T_{\mathrm{SDW}}(p)$ data. This suggests that both transition temperatures are consistent within the experimental uncertainty and exhibit similar pressure dependencies.

V. OXYGEN-ISOTOPE SUBSTITUTION EXPERIMENTS

A. Oxygen-isotope effect on phonon modes

The substitution of the lighter ^{16}O isotope with the heavier ^{18}O is expected to produce systematic downshifts of oxygen-dominated phonons. This effect is indeed observed, as shown in Figs. 1(e) and 1(f), where the Raman lines of

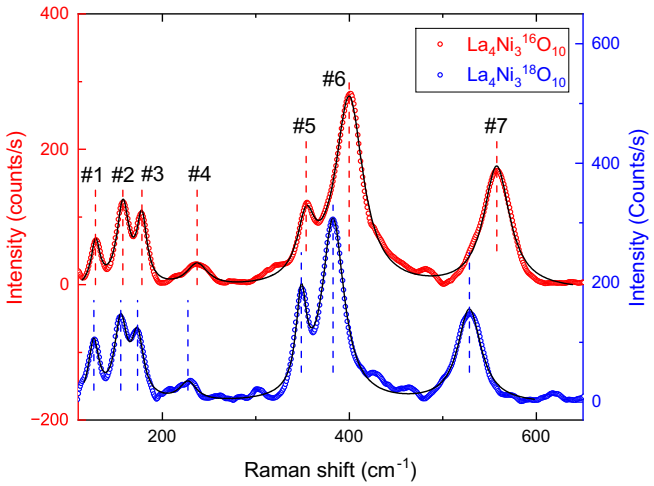

FIG. 6. Room-temperature Raman spectra of oxygen-isotope substituted $La_4Ni_3O_{10}$ samples. Solid lines represent fits using seven Lorentzian functions. Dashed lines indicate the peak positions.

^{18}O-substituted $La_4Ni_3O_{10}$ appear at lower frequencies compared to those of the ^{16}O-substituted and pristine samples.

The room-temperature Raman spectra of the ^{16}O- and ^{18}O-substituted $La_4Ni_3O_{10}$ samples were analyzed by fitting the seven most pronounced Raman lines with Lorentzian functions (see Fig. 6). Note that the spectra in Fig. 6 were collected at different laser-beam positions than those shown in Fig. 1(e). Variations in relative intensities arise from the polycrystalline nature of the sample. Because of the relatively small laser spot size ($\simeq$2 μm), the Raman response is highly sensitive to the orientation of the illuminated grains. The Raman wave numbers (ν^{16} and ν^{18}), averaged over six different measurements, are summarized in Table III.

The isotope dependence of the Raman wave numbers ν^{16} and ν^{18} was analyzed using a partial mass-scaling formalism developed in Refs. [62–64]:

$$\nu(x) = \nu^{16}\left(\sqrt{\frac{16}{\bar{M}(x)}}\right)^{f_{\mathrm{O}}}, \quad \bar{M}(x) = 16(1-x) + 18x. \quad (2)$$

Here, x is the ^{18}O fraction, ν^{16} is the frequency in the pure ^{16}O sample, $\bar{M}$ is the average oxygen mass in the partially ^{18}O-substituted sample, and f_{O} is the oxygen participation parameter. Taking logarithms gives

$$f_{\mathrm{O}} = \frac{\ln(\nu(x)/\nu^{16})}{\ln(\sqrt{16/\bar{M}(x)})} = \frac{\ln(1+s)}{\ln(\sqrt{16/\bar{M}(x)})}, \quad (3)$$

with the fractional shift $s = \nu^{18}/\nu^{16} - 1$. For an ^{18}O isotope fraction of $x \simeq 82\%$, the values of the oxygen participation parameter f_{O} were calculated and are summarized in Table III and Fig. 7. The experimentally observed Raman frequencies were assigned to the calculated phonon modes reported in Ref. [47] and its Supplemental Material (see the last two columns of Table III). Comparison of the measured and theoretical values leads to the following conclusions:

(1) The Raman lines near 558, 400, and 240 cm^{-1} are assigned predominantly to oxygen vibrations, which is

TABLE III. Raman-active phonon frequencies (ν^{16}/ν^{18}), fractional shift (s), and oxygen participation factor (f_O) in ^{16}O- and ^{18}O-substituted $La_4Ni_3O_{10}$ at 300 K. Theoretical frequencies (ν^{calc}) and assigned phonon modes are from Ref. [47] [see Figs. 2(f)–2(j) and the Supplemental Material therein].

ν^{16} (cm^{-1})	ν^{18} (cm^{-1})	s	f_O	ν^{calc} (cm^{-1})	Assignment
129.3(1)	126.1(1)	−0.017(3)	0.76(15)	127.2[a]	Collective bending involving apical and planar oxygens together with La/Ni.[a]
157.4(1)	154.8(1)	−0.017(3)	0.75(12)	164.1[a]	Ni and apical-oxygen motion within Ni–O and *ab* planes.[a]
182.5(1)	173.5(1)	−0.025(6)	0.48(11)	182.5[a]	Mixed apical-oxygen displacements (in-plane and *c*), accompanied by Ni and La motion.[a]
239.6(1)	223.9(1)	−0.054(12)	1.15(26)	239.6[a]	Apical-oxygen dominated vibration along *c*, with additional planar-oxygen contribution.[a]
353.7(1)	348.7(1)	−0.014(5)	0.29(10)	349.3[a]	Apical-oxygen and Ni displacements (outer layers), mixed in-plane/*c*-axis character.[a]
399.7(1)	382.7(1)	−0.043(3)	0.90(6)	396.3[a]	Planar-oxygen quadrupolar stretch (outer planes), vibrations within the *ab* plane.[a]
557.8(1)	528.4(1)	−0.053(3)	1.11(6)	554.9[a]	High-energy O stretch, dominated by apical/planar oxygen displacements mainly along *c* axis.[a]

[a]From density-functional perturbation theory (DFPT) calculations reported in Ref. [47] [see Figs. 2(f)–2(j) and the Supplemental Material therein, where all Raman-active modes of $La_4Ni_3O_{10}$ are listed].

consistent with the oxygen participation factor being close to unity ($f_O \simeq 1.0$, see Fig. 7).

(2) Modes involving La and Ni motion (near 129, 157, 183, and 354 cm^{-1}) exhibit reduced oxygen participation, with $f_O < 1$.

It is noteworthy that for the oxygen-dominated modes (near 558, 400, and 240 cm^{-1}), both apical and planar oxygens contribute to the vibrations, resulting in $f_O \simeq 1.0$ (see the last two columns in Table III and Fig. 7). This strongly suggests a uniform distribution of ^{18}O throughout the sample. The ratio of ≃20% ^{16}O to ≃80% ^{18}O appears to remain constant across all oxygen sites (apical, inner planes, and outer planes).

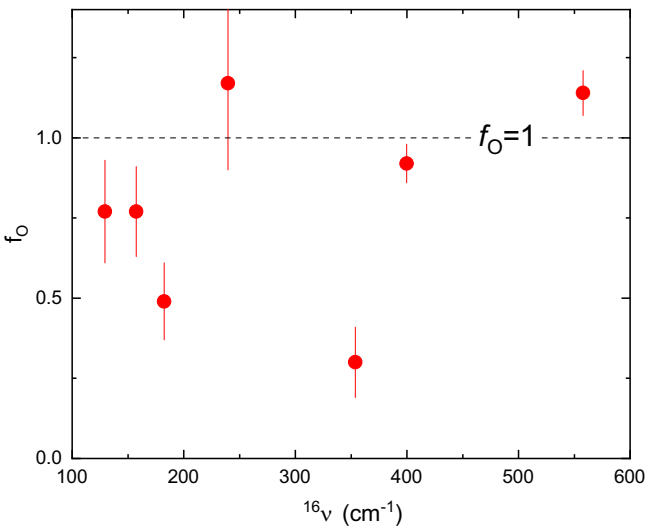

FIG. 7. The oxygen participation parameter f_O as a function of the Raman wave number ν^{16}.

B. Oxygen-isotope effect on the spin-density-wave transitions

Figures 8(a)–8(c) present time spectra collected in WTF-μSR experiments for ^{16}O- and ^{18}O-substituted $La_4Ni_3O_{10}$ samples. At $T = 10$ K [panel (a)], the oscillations in B_{WTF} are strongly suppressed, indicating that both samples remain in the magnetic state. At $T = 132.5$ K [panel (b)], the asymmetries are partially recovered, reaching approximately half of the full amplitude, with a slightly higher absolute value for the La_4Ni_3 $^{16}O_{10}$ sample compared to the La_4Ni_3 $^{18}O_{10}$ one. This suggests that the magnetic volume fraction f_m is higher in the ^{18}O-substituted sample than in the ^{16}O-substituted one. Above the SDW transition [$T = 210$ K, panel (c)], the asymmetries for both samples become equal and reach a maximum value of approximately 0.27, consistent with the characteristics of the GPS μSR spectrometer [65].

The temperature evolution of the magnetic volume fractions obtained from fits to the WTF-μSR data is presented in Fig. 8(d). Figure 8(e) shows an expanded view of the $f_m(T)$ curves in the vicinity of T_{SDW}. The T_{SDW} transition temperatures were estimated from the intersection of the linearly extrapolated $f_m(T)$ curves near T_{SDW} with the reference line $f_m(T) = 0.5 \times f_m(10\,K)$. The fits yield an isotope shift of T_{SDW} as $T^{18}_{SDW} - T^{16}_{SDW} = 2.1(1)$ K.

The OIE on the spin-reorientation transition temperature T^* was further investigated in ZF-μSR experiments. The magnetic field distributions measured in the pristine $La_4Ni_3O_{10}$ sample, shown in Figs. 2(c)–2(e), as well as those for the isotope-substituted samples in Figs. 8(f) and 8(g), suggest that the spin-reorientation transition at T^* is characterized by the disappearance of components #1, #3, and #5. The most pronounced changes occur in component #5, which is among the strongest below T^* but disappears above it, and in component #4, whose intensity nearly doubles above T^*. The corresponding temperature dependencies of the volume fractions $f_{m,4}$ and $f_{m,5}$ are shown in Figs. 8(h) and 8(i).

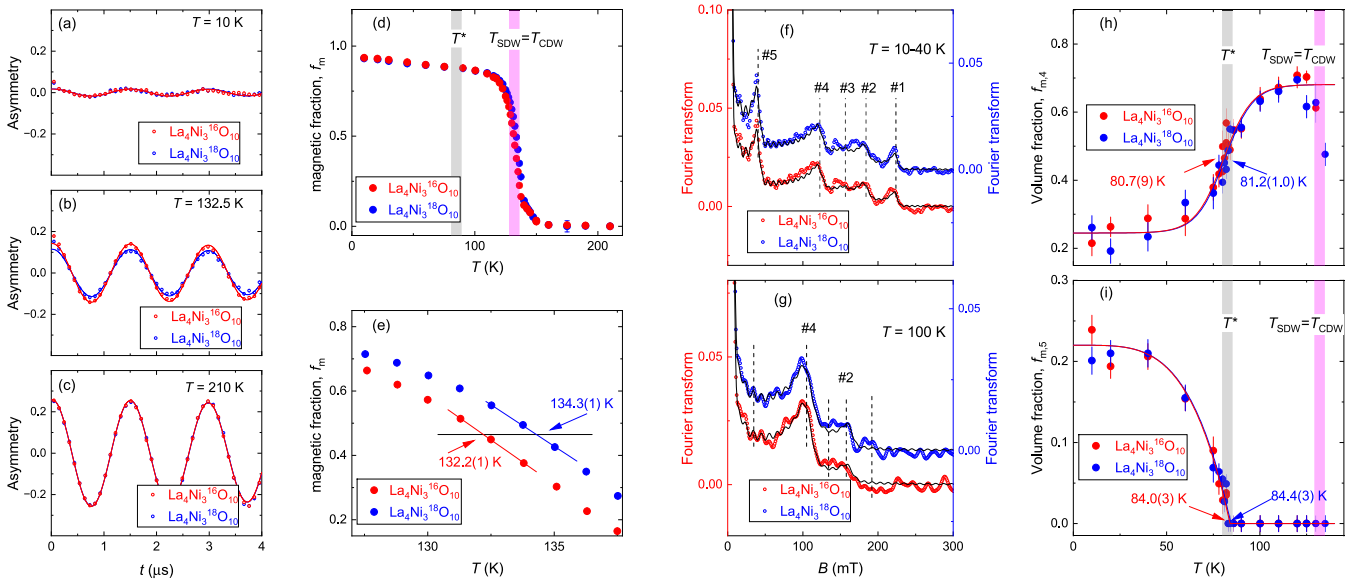

FIG. 8. (a)–(c) WTF-μSR time spectra of $^{16}O/^{18}O$-substituted $La_4Ni_3O_{10}$ samples measured at $T = 10$, 132, and 210 K, respectively. (d) Temperature dependence of the magnetic volume fraction f_m for $^{16}O/^{18}O$-substituted $La_4Ni_3O_{10}$ samples. The gray and pink stripes represent $T_{SDW} = T_{CDW}$ and T^*, respectively, as obtained from μSR and resistivity studies of the pristine $La_4Ni_3O_{10}$ sample [see Figs. 2 and 4, and Secs. III and IV]. (e) Expanded view of the $f_m(T)$ curves in the vicinity of the SDW transitions. Distribution of internal fields in $^{16}O/^{18}O$-substituted $La_4Ni_3O_{10}$ samples, collected at temperatures ranging from 10 to 40 K [panel (f)] and at $T = 100$ K [panel (g)]. Dashed lines represent the positions of the five-field components. (h) Temperature dependence of the magnetic volume fraction $f_{m,4}$. Solid lines are fits to the data using Eq. (4). (i) Temperature dependence of $f_{m,5}$. Solid lines represent fits using Eq. (5).

The solid lines in Figs. 8(h) and 8(i) correspond to fits of the following models to the $f_{m,4}(T)$ and $f_{m,5}(T)$ data:

$$f_{m,4}(T) = f_{m,0} - \Delta f_{m,4}\left[1 + \exp\left(\frac{T^* - T}{\Delta T^*}\right)\right]^{-1} \quad (4)$$

and

$$f_{m,5}(T) = \begin{cases} f_{m,high}\,, & T > T^*, \\ f_{m,high} + \Delta f_{m,5}\left[1 - \left(\frac{T}{T^*}\right)^n\right], & T < T^*. \end{cases} \quad (5)$$

Here, $f_{m,0}$ and $f_{m,high}$ represent the volume fractions at $T = 0$ and $T > T^*$, respectively, and $\Delta f_m = f_{m,0} - f_{m,high}$ denotes the transition amplitude. ΔT^* characterizes the width of the transition, while n is the exponent. To reduce correlation between parameters, the fits were performed by assuming equal values of $f_{m,0}$, Δf_m, and ΔT^* in Eq. (4), and equal values of $f_{m,high}$ and Δf_m in Eq. (5) for both ^{16}O- and ^{18}O-substituted samples, while keeping T^* isotope dependent. The fits confirm the absence of a measurable isotope shift in the spin-reorientation transition temperature T^* within the experimental accuracy. The estimated shifts in the T^* transition temperatures were found to be $T^{*,18} - T^{*,16} = 0.5(1.3)$ and 0.4(4) K from the fits to $f_{m,4}(T)$ and $f_{m,5}(T)$ data sets, respectively.

It should be noted that the determination of the spin-reorientation transition temperature T^* depends on the choice of the model function—Eqs. (4) and (5) in our case—which may introduce relatively high uncertainties in the absolute value of T^* [≃81 or ≃84 K, as shown in Figs. 8(h) and 8(i)]. On the other hand, fitting Eqs. (4) and (5) to $f_{m,4}(T)$ and $f_{m,5}(T)$ data yields considerably smaller statistical errors, implying that uncertainties in the relative change of T^* are low. The magnetic ordering temperatures determined for the pristine and $^{16}O/^{18}O$-substituted samples investigated in the present study are summarized in Table IV. The temperature dependencies of $f_m(T)$, and individual volume fraction components [$f_{m,1}(T)$ to $f_{m,5}(T)$] for pristine $La_4Ni_3O_{10}$, obtained from WTF- and ZF-μSR studies, are presented in the Supplemental Material [49]. The larger uncertainties in T_{SDW} and T^* for the pristine sample arise from the coarser temperature steps used in the corresponding μSR experiments. Despite these larger uncertainties, the value of T_{SDW} for the pristine sample remains closer to that of the ^{16}O-substituted sample than to the ^{18}O-substituted one, as might be expected. The spin-reorientation temperature T^* for the pristine sample also exhibits a higher uncertainty compared to the values obtained from fine temperature-step measurements on $La_4Ni_3\ ^{16}O_{10}$ and $La_4Ni_3\ ^{18}O_{10}$, but it remains within the same temperature range.

C. Oxygen-isotope effect on the charge-density-wave transitions

The OIE on the CDW transition temperature was investigated by resistivity measurements. Figure 1(f) shows the temperature dependence of the resistivity normalized to its 300 K value, $R(T)/R(300)$. The raw resistivity curves exhibit weakly pronounced features at $T \sim 130$ K for all three $La_4Ni_3O_{10}$ samples. A more distinct structure becomes evident upon taking the first derivative of the resistivity data, as shown in Fig. 9(a).

Figure 9(b) presents an expanded view of the resistivity derivative curves near the CDW ordering temperatures. The CDW transition temperature was determined from the intersection point of linear fits to the derivative curves near the local minimum. Clearly, the CDW transition temperatures

TABLE IV. The spin-density-wave (T_{SDW} and T^*) and the charge-density-wave (T_{CDW}) transition temperatures obtained at pristine and oxygen-isotope-substituted $La_4Ni_3O_{10}$ samples. $T_{tr}^{18} - T_{tr}^{16}$ denotes isotope shift of the transition temperature ($T_{tr} = T_{CDW}$, T^*, or T_{SDW}). The oxygen isotope exponent $\alpha = -\mathrm{d}\ln T_{tr}/\mathrm{d}\ln M$ (M is the mass of the oxygen isotope) is corrected for uncomplete isotope exchange $\simeq$82%.

	$La_4Ni_3O_{10}$ (K)	$La_4Ni_3\ ^{16}O_{10}$ (K)	$La_4Ni_3\ ^{18}O_{10}$ (K)	$T_{tr}^{18} - T_{tr}^{16}$ (K)	α	Technique
T_{CDW}	136.0(1)	135.8(1)	138.0(1)	2.2(1)	−0.16(1)	Resistivity
T_{SDW}	131.3(4)	132.2(1)	134.3(1)	2.1(1)	−0.15(1)	WTF-μSR
	131.8(4)					ZF-μSR
T^*	82.2(2.4)[a]	80.7(9)[a]	81.2(1.0)[a]	0.5(1.3)	−0.06(16)	ZF-μSR
	83.1(1.3)[b]	84.0(3)[c]	84.4(3)[c]	0.4(0.4)	−0.05(5)	ZF-μSR

[a]From the fit of Eq. (4) to $f_{m,4}(T)$ data.
[b]From the fit of Eq. (5) to $f_{m,1}(T)$ data.
[c]From the fit of Eq. (5) to $f_{m,5}(T)$ data.

for the pristine and ^{16}O-substituted $La_4Ni_3O_{10}$ samples remain nearly the same, while T_{CDW} for $La_4Ni_3\ ^{18}O_{10}$ is shifted to higher temperatures. The T_{CDW} values for the pristine and oxygen-isotope-substituted samples are summarized in Table IV.

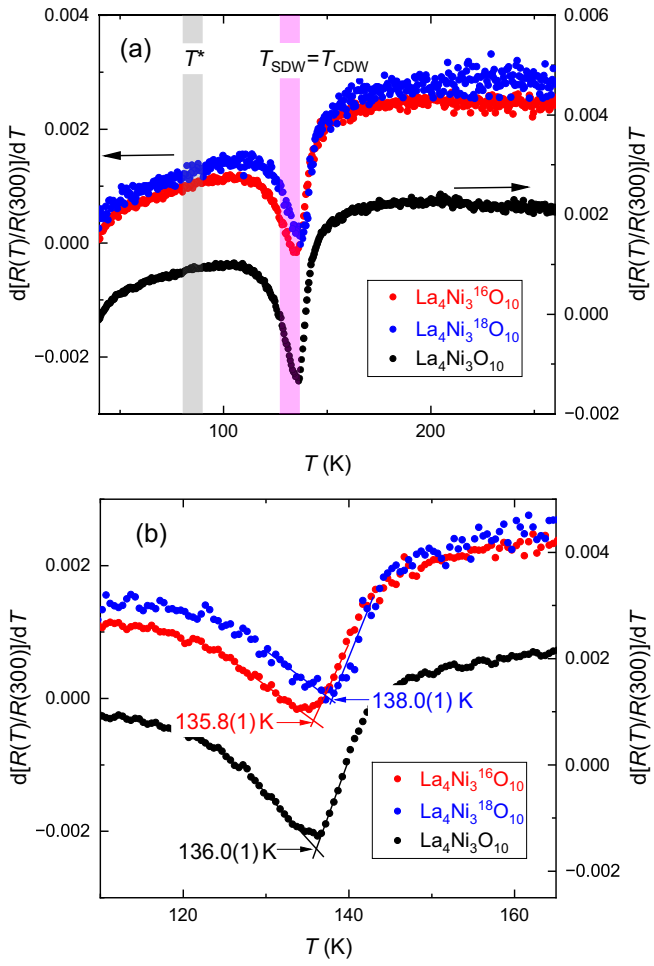

FIG. 9. (a) First derivatives of the resistivity curves for pristine and isotope-substituted $La_4Ni_3O_{10}$ samples. (b) Expanded view of the derivative curves in the vicinity of the CDW transition.

VI. CONCLUSIONS AND OUTLOOK

This study investigates the three-layer Ruddlesden-Popper nickelate $La_4Ni_3O_{10}$ using μSR and resistivity, offering comprehensive insights into the interplay between spin and charge orders under both ambient- and high-pressure conditions, as well as the effects induced by substituting ^{16}O with its heavier isotope ^{18}O.

At ambient pressure, two magnetic transitions are identified at $T_{SDW} \simeq 132$ K and $T^* \simeq 80$–90 K. The incommensurate nature of both magnetic states is confirmed by zero-field μSR experiments through the observation of an Overhauser-type magnetic field distribution in the frequency domain (corresponding to a zeroth-order Bessel function in the time domain). An abrupt onset of internal fields indicates a first-order-like character of the transition at T_{SDW}.

Muon stopping site and dipole-field calculations suggest the presence of a small Ni magnetic moment on the inner Ni-O layers and indicate that the magnetic moments likely lie within the *ab* plane above T^*, gradually acquiring a *c*-axis component at lower temperatures.

The CDW order is evidenced by an anomaly in the resistivity curve, with T_{CDW} coinciding with T_{SDW}, consistent with previous studies [2].

Under applied pressure, both resistivity and μSR measurements reveal the suppression of all transitions, including the two magnetic transitions (T_{SDW} and T^*) and the CDW transition. The pressure coefficients for these transitions are nearly identical, $\simeq -13$ K/GPa, and the SDW and CDW transitions remain closely intertwined under increasing pressure. The onset of magnetic ordering ($T_{m,onset}$) decreases more slowly than the SDW ordering temperature, suggesting that magnetic fluctuations—acting as precursors to static magnetic order and detectable by μSR—are effectively enhanced under pressure.

The resulting phase diagram, presented in Fig. 10, highlights the suppression of density-wave transitions with increasing pressure. Interestingly, $T_{m,onset}$ appears to follow the pressure dependence of the density-wave transition observed in ultrafast optical pump-probe spectroscopy experiments [9]. Considering the difference in time scales between μSR and femtosecond optical spectroscopy (10^{-5}–10^{-10} s for μSR vs $\sim 10^{-15}$ s for femtosecond spectroscopy), one may assume that magnetic fluctuations which remain dynamic on the muon time scale could be detected as static order at the femtosecond

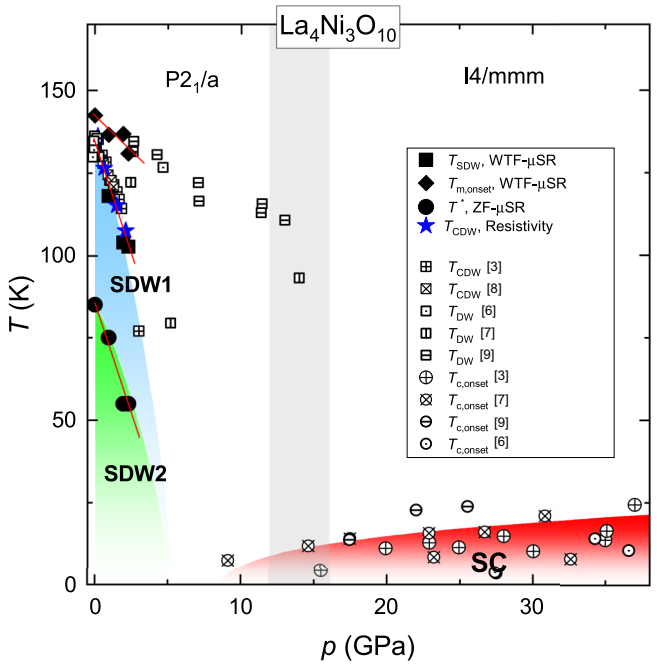

FIG. 10. The pressure-temperature (p-T) phase diagram of $La_4Ni_3O_{10}$. Solid symbols represent the pressure dependencies of the magnetic ordering temperatures $T_{m,onset}$, T_{SDW}, and T^*, as obtained from ZF- and WTF-μSR experiments (black squares and circles) and the CDW ordering temperature (T_{CDW}) derived from resistivity studies (blue stars) in the present work. The open squares and circles denote the T_{CDW} vs p and the onset of the superconducting transition temperature T_c vs p data from Refs. [3,6–9].

scale. We cannot exclude, however, that the coincidence between $T_{m,onset}$ and T_{DW} reported in Ref. [9] is accidental.

The simultaneous suppression of density-wave transitions in $La_4Ni_3O_{10}$ contrasts with the behavior of the two-layer RP nickelate $La_3Ni_2O_7$ [13], where external pressure enhances the separation between the SDW and CDW transitions. The differing pressure responses of $La_3Ni_2O_7$ and $La_4Ni_3O_{10}$ arise from the fact, that in $La_3Ni_2O_7$ the SDW and CDW orders are decoupled, allowing the SDW transition to be independently enhanced under pressure. Lattice compression likely strengthens exchange interactions between neighboring Ni moments, thereby increasing the SDW transition temperature.

In contrast, in $La_4Ni_3O_{10}$ the SDW and CDW orders are strongly coupled and intertwined [2], meaning that the SDW transition is highly dependent on the stability of the CDW. As pressure suppresses the CDW order, it simultaneously destabilizes the SDW, leading to a reduction in the SDW transition temperature. This contrast highlights the critical role of SDW–CDW coupling in determining the pressure response: $La_4Ni_3O_{10}$ exhibits mutual destabilization of both orders under pressure, whereas $La_3Ni_2O_7$ allows the SDW order to evolve more independently. It should be noted, however, that ultrafast optical studies on both $La_3Ni_2O_7$ [66] and $La_4Ni_3O_{10}$ [9] show that SDW order is suppressed prior to the onset of superconductivity. This suggests that, while the double- and triple-layer nickelates display distinct behaviors at low pressures, their phase diagrams may converge as one approaches the superconducting regime at higher pressures.

The interpretation on the critical role of SDW–CDW coupling is further supported by OIE experiments. In $La_4Ni_3O_{10}$, where SDW and CDW orders are coupled and both break lattice translational symmetry, the OIE on both T_{SDW} and T_{CDW} is nearly identical. However, when the magnetic transition is decoupled from the CDW order—as in the case of the spin-reorientation transition at T^* —no additional lattice translational symmetry is broken, and the isotope effect on the corresponding magnetic ordering temperature remains negligible.

The relationship between spin and charge orders in $La_4Ni_3O_{10}$ mirrors the intricate interplay observed in cuprates [34–40] and hole-doped nickelates such as $La_{2-x}Sr_xNiO_4$ [42,43]. In these systems, spin and charge orders are strongly intertwined and exhibit similar responses to external perturbations. However, important open questions remain: Why does the magnetic order change from commensurate to incommensurate as one moves from the two-layer to the three-layer RP nickelate system? What drives the pressure-enhanced separation of SDW and CDW transitions observed in $La_3Ni_2O_7$, in contrast to the intertwined behavior seen in $La_4Ni_3O_{10}$? Addressing these questions will require further experimental and theoretical investigations into the electronic structure and magnetic interactions of RP nickelates under varying conditions.

While finalizing this paper, we became aware of a report on ambient-pressure μSR studies of $La_4Ni_3O_{10}$ [67], which reports the observation of a second magnetic transition around 70–100 K, accompanied by a change in the magnetic field distribution.

ACKNOWLEDGMENTS

This work is based on experiments performed at the Swiss Muon Source SμS, Paul Scherrer Institute, Villigen, Switzerland. R.K. acknowledges the authors of Ref. [47] for providing theoretical Raman data prior to publication, M. Hepting for helpful discussions, and J. Mitchell and D. Phelan for supplying neutron data on $Pr_4Ni_3O_{10}$. Z.G. acknowledges support from the Swiss National Science Foundation (SNSF) through SNSF Starting Grant (No. TMSGI2_211750). I.P. acknowledges financial support from Paul Scherrer Institute research Grant No. 2021_0134. D.J.G. acknowledges support from the Swiss National Science Foundation (SNSF) through Grant No. 238113.

DATA AVAILABILITY

The data are available from the authors upon reasonable request.

APPENDIX: MATERIALS AND METHODS

1. Sample preparation

The $La_4Ni_3O_{10}$ polycrystalline sample was synthesized using a combination of mechanosynthesis and solid-state reaction method, similar to that described in Ref. [13]. The starting materials were La_2O_3 (5N, Sigma-Aldrich) and NiO (4N8, Alfa Aesar). Prior to synthesis, La_2O_3 and NiO were dried at 1200 and 280 °C, respectively, for 12 h. Stoichiometric amounts of freshly dried La_2O_3 (21.490 g, 65.96 mmol)

and NiO (7.390 g, 10.0 mmol) were well mixed in RM 100 (Retsch®) mechanical mortar. The mixture of oxides was divided into two aliquots and placed together with 10 mm balls in a 45 ml agate grinding bowl and then subjected to mechanosynthesis in a PULVERISETTE 7 planetary micro ball-mill (Fritsch GmbH) during 20 cycles at 600 rpm for 5 min milling and 5 min cooling conditions. The resulting black precursor powder was cold-pressed into a pellet by applying 4000 bar uniaxial pressure and annealed in oxygen (5N, PabGas) under 200 ml/min flow at 1100 °C for 10 h, followed by a final thermal treatment performed at 500° for 6 h.

Approximately 1.0 g of $La_4Ni_3O_{10}$ initial material in a powder from was used for the isotope exchange process. The sample was divided into two equal parts (≃0.5 g each) and placed in ampules filled with $^{18}O_2$ (Euriso-Top, 97.1% enrichment) and a mixture of natural isotopes of oxygen, hereafter referred to $^{16}O_2$ (PanGas, 5N), respectively. The experimental setup is described in Refs. [68,69]. The samples were annealed simultaneously in $^{16}O_2$ and $^{18}O_2$ atmospheres in small overpressure (up to ∼1.5 bar) at $T = 1000$ °C for 6 h, followed by a postannealing step at $T = 500$ °C for 24 h. To increase the isotope content in the ^{18}O-substituted samples, $^{18}O_2$ gas was replaced and the OIE procedure was repeated four times. Since the mass spectrometer is coupled to the isotopic oxygen reactor, the isotope exchange rate can be monitored in situ and estimated based on simple reaction progress and equilibrium constants dependencies [70]. The ^{18}O content in $La_4Ni_3\,{}^{18}O_{10}$ sample is thus derived to be 82(2)%.

2. μSR experiments

The ambient-pressure and high-pressure muon-spin rotation/relaxation (μSR) experiments were conducted at the πM3 and μE1 beamlines at the Paul Scherrer Institute (PSI Villigen, Switzerland), using the dedicated GPS (General Purpose Surface, Ref. [65]) and GPD (General Purpose Decay, Refs. [61,71]) muon spectrometers. Quasihydrostatic pressures of up to ≃2.3 GPa were generated using double-wall piston-cylinder clamp cells made of the nonmagnetic MP35N alloy [61]. The μSR data were analyzed using the MUSRFIT software package [72]. The μSR experiments were performed in two modes. In the first mode, ZF-μSR measurements were conducted without applying an external magnetic field. In the second mode, a WTF was applied perpendicular to the initial muon-spin polarization.

3. ZF-μSR and WTF-μSR data analysis procedure

The experimental μSR data were fitted using the following functional form:

$$A(t) = A_{0,\mathrm{s}} P_{\mathrm{s}}(t) + A_{0,\mathrm{bg}} P_{\mathrm{bg}}(t), \tag{A1}$$

where the subscripts s and bg denote the sample and background contributions, respectively, and A_0 and P represent the initial asymmetry and the time evolution of the muon-spin polarization, respectively. The sample polarization function, $P_{\mathrm{s}}(t)$, was further divided into magnetic (m) and nonmagnetic (nm) components, with corresponding weights f_{m} and $1 - f_{\mathrm{m}}$. In experiments conducted on the low-background GPS muon spectrometer [65], the background contribution was found to be negligible ($A_{0,\mathrm{bg}} \simeq 0$). In μSR experiments under pressure performed at GPD muon instrument [61,71], the background arises from muons stopped in the pressure cell walls and accounts for approximately 50% of the total μSR response.

In ZF-μSR experiments, the magnetic (m) and nonmagnetic (nm) contributions to the sample muon-spin polarization function $P_{\mathrm{s}}(t)$ were obtained as

$$P_{\mathrm{s,m}}(t) = \frac{2}{3} \sum_i f_{\mathrm{m},i} e^{-\lambda_{\mathrm{T},i} t} J_0(\gamma_\mu B_{\mathrm{int},i} t) + \frac{1}{3} e^{-\lambda_{\mathrm{L}}} \tag{A2}$$

and

$$P_{\mathrm{s,nm}}(t) = \frac{2}{3}(1 - \sigma_{\mathrm{GKT}}^2 t^2) \exp\left[-\frac{\sigma_{\mathrm{GKT}}^2 t^2}{2}\right] + \frac{1}{3}, \tag{A3}$$

where J_0 is the zeroth-order Bessel function, $\gamma_\mu = 851.616$ MHz/T is the muon gyromagnetic ratio, λ represents the exponential relaxation rates, σ_{GKT} is the Gaussian Kubo-Toyabe relaxation rate, and $f_{\mathrm{m},i}$s are the volume fractions of individual magnetic components ($\sum f_{\mathrm{m},i} = f_{\mathrm{m}}$). The coefficients 2/3 and 1/3 account for powder averaging, with 2/3 of the muon spins precessing in internal fields perpendicular (transverse, T) to the field direction and 1/3 remaining parallel (longitudinal, L) to $B_{\mathrm{int},i}$ [50–52,73].

The WTF sample response was modeled as

$$P_{\mathrm{s}}(t) = f_{\mathrm{m}}\left[\tfrac{2}{3} e^{-\lambda_{\mathrm{T}} t} + \tfrac{1}{3} e^{-\lambda_{\mathrm{L}} t}\right] + (1 - f_{\mathrm{m}}) e^{-\sigma_{\mathrm{WTF}}^2 t^2/2} \cos(\gamma_\mu B_{\mathrm{WTF}} t + \phi), \tag{A4}$$

where ϕ is the initial phase of the muon-spin ensemble, $B_{\mathrm{WTF}} = 5$ mT is the weak transverse field, and σ_{WTF} is the Gaussian relaxation rate of the nonmagnetic component. The first term in Eq. (A4) corresponds to Eq. (A2), where, due to data binning, all oscillating components are combined into a single decay term. The second term describes muon-spin precession in B_{WTF} within the nonmagnetic phase of the sample.

4. Muon stopping sites and dipole-field calculations

Muon stopping sites were calculated using a DFT + μ approach [74] using the MuFinder application [75]. Density functional theory calculations were performed using the plane-wave pseudopotential code CASTEP [76]. The PBEsol functional [77] was used in all calculations. Calculations were converged to ∼3 meV/atom using a plane-wave cutoff of 800 eV and a 3 × 3 × 3 k-point grid [78]. Fifty-four calculations were performed, each where a muon was implanted randomly into a cell of approximately 11 Å × 11 Å × 14 Å. The atomic positions were subsequently allowed to relax until the energy and atomic positions had converged to better than 2×10^{-2} meV/atom and 1×10^{-3} Å, respectively, and the maximum force on any atom was less than 5×10^{-2} eV/Å. The final muon positions were clustered using the MUFINDER application to give the candidate muon stopping sites, which were subsequently used in the MUESR code [79] to calculate the dipolar field at these sites for candidate magnetic structures. To capture the effect of an incommensurate magnetic structure, such as a spin-density wave, many calculations

with the initial phase of the magnetic structure varied were performed.

5. Resistivity experiments

Experiments under ambient pressure were performed by using the "Resistivity" option hardware and software of the quantum design physical property measurement system (PPMS). Experiments under pressure were performed using the same PPMS instrument by using Almax Easylab Pcell 15/30 module [80].

6. Neutron powder diffraction experiments

NPD experiments were carried out using the high-intensity cold neutron diffractometer DMC (neutron wavelength $\lambda_n = 3.82$ Å) and the high-resolution thermal neutron diffractometer HRPT ($\lambda_n = 2.45$ Å), both located at the spallation neutron source SINQ (PSI Villigen, Switzerland) [81,82]. A ca. 9 g sample was loaded into an 8-mm V-container for use in the measurements. The diffraction data were analyzed using the Rietveld refinement program JANA [83].

7. Raman experiments

Raman spectra were collected using a LabRAM Series Raman Microscope (Horiba Jobin Yvon) with a He–Ne excitation laser ($\lambda = 632.8$ nm, ∼20 mW). The scattered light was dispersed by an 1800 grooves mm^{-1} grating, and an edge filter suppressed the laser line. A 50× objective was used, with the laser intensity reduced by a factor of 100 to avoid sample heating. Measurements were performed at multiple locations, as the grain size was comparable to the laser spot (≃2 μm), and 20–50 scans were typically averaged to improve statistics. Background subtraction was carried out using the Jobin Yvon software.

8. Other experimental techniques

Laboratory x-ray powder diffraction was performed at room temperature in the Bragg-Brentano geometry using a Bruker AXS D8 Advance diffractometer (Bruker AXS GmbH, Karlsruhe, Germany) equipped with a Ni-filtered Cu Kα radiation and a 1D LynxEye PSD detector to confirm the phase-purity. Le Bail analysis of the obtained diffraction pattern was performed using the FULLPROF Suite package [84].

Thermogravimetric analysis (TGA) hydrogen reduction was performed to elucidate the oxygen content in the resulting $La_4Ni_3O_{10-\delta}$ samples. A NETZSCH STA 449F1 simultaneous thermal analyzer (STA) was used for the thermogravimetry experiments. The gas used in the experiment was a mixture of 5 vol.% of hydrogen (Messer Schweiz AG, 5N) in helium (PanGas, 6N).

Field-cooled magnetization experiments were performed by using SQUID magnetometer Quantum Design MPMS-5 over a wide range of applied fields, from 20 mT to 5 T.

[1] H. Sun, M. Huo, X. Hu, J. Li, Z. Liu, Y. Han, L. Tang, Z. Mao, P. Yang, B. Wang, J. Cheng, D.-X. Yao, G.-M. Zhang, and M. Wang, Signatures of superconductivity near 80 K in a nickelate under high pressure, Nature (London) **621**, 493 (2023).

[2] J. Zhang, D. Phelan, A. S. Botana, Y.-S. Chen, H. Zheng, M. Krogstad, S. G. Wang, Y. Qi, J. A. Rodriguez-Rivera, R. Osborn, S. Rosenkranz, M. R. Norman, and J. F. Mitchell, Intertwined density waves in a metallic nickelate, Nat. Commun. **11**, 6003 (2020).

[3] Y. Zhu, *et al.*, Superconductivity in pressurized trilayer $La_4Ni_3O_{10-\delta}$ single crystals, Nature (London) **631**, 531 (2024).

[4] H. Sakakibara, M. Ochi, H. Nagata, Y. Ueki, H. Sakurai, R. Matsumoto, K. Terashima, K. Hirose, H. Ohta, M. Kato, Y. Takano, and K. Kuroki, Theoretical analysis on the possibility of superconductivity in the trilayer Ruddlesden-Popper nickelate $La_4Ni_3O_{10}$ under pressure and its experimental examination: Comparison with $La_3Ni_2O_7$, Phys. Rev. B **109**, 144511 (2024).

[5] M. Wang, H.-H. Wen, T. Wu, D.-X. Yao, and T. Xiang, Normal and superconducting properties of $La_3Ni_2O_7$, Chin. Phys. Lett. **41**, 077402 (2024).

[6] Q. Li, Y.-J. Zhang, Z.-N. Xiang, Y. Zhang, X. Zhu, and H.-H. Wen, Signature of superconductivity in pressurized $La_4Ni_3O_10$, Chin. Phys. Lett. **41**, 017401 (2024).

[7] M. Zhang, *et al.*, Superconductivity in trilayer nickelate $La_4Ni_3O_{10}$ under pressure, Phys. Rev. X **15**, 021005 (2025).

[8] G. Wu, J. J. Neumeier, and M. F. Hundley, Magnetic susceptibility, heat capacity, and pressure dependence of the electrical resistivity of $La_3Ni_2O_7$ and $La_4Ni_3O_{10}$, Phys. Rev. B **63**, 245120 (2001).

[9] S. Xu, H. Wang, M. Huo, D. Hu, Q. Wu, L. Yue, D. Wu, M. Wang, T. Dong, and N. Wang, Collapse of density wave and emergence of superconductivity in pressurized-$La_4Ni_3O_{10}$ evidenced by ultrafast spectroscopy, Nat. Commun. **16**, 7039 (2025).

[10] S. Huangfu, X. Zhang, and A. Schilling, Correlation between the tolerance factor and phase transition in $A_{4-x}B_xNi_3O_{10}$ (A and B = La, Pr, and Nd; $x = 0, 1, 2, 3$), Phys. Rev. Res. **2**, 033247 (2020).

[11] H. Li, X. Zhou, T. Nummy, J. Zhang, V. Pardo, W. E. Pickett, J. F. Mitchell, and D. S. Dessau, Fermiology and electron dynamics of trilayer nickelate $La_4Ni_3O_{10}$, Nat. Commun. **8**, 704 (2017).

[12] J. Zhang, H. Zheng, Y.-S. Chen, Y. Ren, M. Yonemura, A. Huq, and J. F. Mitchell, High oxygen pressure floating zone growth and crystal structure of the metallic nickelates $R_4Ni_3O_{10}$ (R = La, Pr), Phys. Rev. Mater. **4**, 083402 (2020).

[13] R. Khasanov, T. J. Hicken, D. J. Gawryluk, L. P. Sorel, S. Bötzel, F. Lechermann, I. M. Eremin, H. Luetkens, Z. Guguchia, Pressure-induced split of the density wave transitions in $La_3Ni_2O_{7-\delta}$, Nat. Phys. **21**, 430 (2025).

[14] N. Wang, *et al.*, Bulk high-temperature superconductivity in pressurized tetragonal $La_2PrNi_2O_7$, Nature (London) **634**, 579 (2024).

[15] M. Shi, D. Peng, K. Fan, Z. Xing, S. Yang, Y. Wang, H. Li, R. Wu, M. Du, B. Ge, Z. Zeng, Q. Zeng, J. Ying, T. Wu, and X. Chen, Superconductivity of the hybrid Ruddlesden-Popper

$La_5Ni_3O_{11}$ single crystals under high pressure, Nat. Phys. **21**, 1780 (2025).

[16] M. Li, J. Gong, Y. Zhu, Z. Chen, J. Zhang, E. Zhang, Y. Li, R. Yin, S. Wang, J. Zhao, D.-L. Feng, Z. Du, and Y.-J. Yan, Direct visualization of an incommensurate unidirectional charge density wave in $La_4Ni_3O_{10}$, Phys. Rev. B **112**, 045132 (2025).

[17] C. Pei, M. Zhang, D. Peng, S. Huangfu, S. Zhu, Q. Wang, J. Wu, Z. Xing, L. Zhang, Y. Chen, J. Zhao, W. Yang, H. Suo, H. Guo, Q. Zeng, and Y. Qi, Pressure-induced superconductivity in $Pr_4Ni_3O_{10}$ single crystals, Sci. China Phys. Mech. Astron. **69**, 237011 (2026).

[18] E. Zhang, D. Peng, Y. Zhu, L. Chen, B. Cui, X. Wang, W. Wang, Q. Zeng, and J. Zhao, Bulk superconductivity in pressurized trilayer nickelate $Pr_4Ni_3O_{10}$ single crystals, Phys. Rev. X **15**, 021008 (2025).

[19] S. Huangfu, G. D. Jakub, X. Zhang, O. Blacque, P. Puphal, E. Pomjakushina, F. O. von Rohr, and A. Schilling, Anisotropic character of the metal-to-metal transition in $Pr_4Ni_3O_{10}$, Phys. Rev. B **101**, 104104 (2020).

[20] S. Huangfu, Z. Guguchia, D. Cheptiakov, X. Zhang, H. Luetkens, D. J. Gawryluk, T. Shang, F. O. von Rohr, and A. Schilling, Short-range magnetic interactions and spin-glass behavior in the quasi-two-dimensional nickelate $Pr_4N_3O_8$, Phys. Rev. B **102**, 054423 (2020).

[21] M. D. Carvalho, M. M. Cruz, A. Wattiaux, J. M. Bassat, F. M. A. Costa, and M. Godinho, Influence of oxygen stoichiometry on the electronic properties of $La_4Ni_3O_{10\pm\delta}$, J. Appl. Phys. **88**, 544 (2000).

[22] D.-K. Seo, W. Liang, M.-H. Whangbo, Z. Zhang, M. Greenblatt, Electronic band structure and Madelung potential study of the nickelates La_2NiO_4, $La_3Ni_2O_7$, and $La_4Ni_3O_{10}$, Inorg. Chem. **35**, 6396 (1996).

[23] J. Li, C.-Q. Chen, C. Huang, Y. Han, M. Huo, X. Huang, P. Ma, Z. Qiu, J. Chen, X. Hu, L. Chen, T. Xie, B. Shen, H. Sun, D.-X. Yao, and M. Wang, Structural transition, electric transport, and electronic structures in the compressed trilayer nickelate $La_4Ni_3O_{10}$, Sci. China Phys. Mech. Astron. **67**, 117403 (2024).

[24] R. Khasanov, A. Shengelaya, D. Di Castro, E. Morenzoni, A. Maisuradze, I. M. Savić, K. Conder, E. Pomjakushina, A. Bussmann-Holder, and H. Keller, Oxygen isotope effects on the superconducting transition and magnetic states within the phase Diagram of $Y_{1-x}Pr_xBa_2Cu_3O_{7-\delta}$, Phys. Rev. Lett. **101**, 077001 (2008).

[25] Z. Guguchia, R. Khasanov, M. Bendele, E. Pomjakushina, K. Conder, A. Shengelaya, and H. Keller, Negative oxygen isotope effect on the static spin stripe order in superconducting $La_{2-x}Ba_xCuO_4$ ($x = 1/8$) observed by Muon-spin rotation, Phys. Rev. Lett. **113**, 057002 (2014).

[26] A. Shengelaya, G.-M. Zhao, C. M. Aegerter, K. Conder, I. M. Savić, and H. Keller, Giant oxygen isotope effect on the spin glass transition in $La_{2-x}Sr_xCu_{1-z}Mn_zO_4$ as revealed by Muon spin rotation, Phys. Rev. Lett. **83**, 5142 (1999).

[27] G.-M. Zhao, K. K. Singh, and Donald E. Morris, Oxygen isotope effect on Néel temperature in various antiferromagnetic cuprates, Phys. Rev. B **50**, 4112 (1994).

[28] M. Medarde, P. Lacorre, K. Conder, F. Fauth, and A. Furrer, Giant $^{16}O - ^{18}O$ isotope effect on the metal-insulator transition of RNiO$_3$ perovskites (R = Rare earth), Phys. Rev. Lett. **80**, 2397 (1998).

[29] H. Luetkens, M. Stingaciu, Y. G. Pashkevich, P. Lemmens, E. Pomjakushina, K. Conder, and H.-H. Klauss, Oxygen isotope effect on the AFM–FM phase transition of the layered cobaltite $HoBaCo_2O_{5.47}$, J. Magn. Magn. Mater. **310**, 1566 (2007).

[30] E. Amit, A. Keren, J. S. Lord, and P. A. King, Precise measurement of the oxygen isotope effect on the Néel temperature in cuprates, Adv. Condens. Matter Phys. **1**, 178190 (2011).

[31] A. Lanzara, G.-M. Zhao, N. L. Saini, A. Bianconi, K. Conder, H. Keller, and K. A. Müller, Oxygen-isotope shift of the charge-stripe ordering temperature in $La_{2-x}Sr_xCuO_4$ from x-ray absorption spectroscopy, J. Phys.: Condens. Matter **11**, L541 (1999).

[32] Z. Guguchia, D. Sheptyakov, E. Pomjakushina, K. Conder, R. Khasanov, A. Shengelaya, A. Simon, A. Bussmann-Holder, and H. Keller, Oxygen isotope effects on lattice properties of $La_{2-x}Ba_xCuO_4$ ($x = 1/8$), Phys. Rev. B **92**, 024508 (2015).

[33] M. Bendele, F. von Rohr, Z. Guguchia, E. Pomjakushina, K. Conder, A. Bianconi, A. Simon, A. Bussmann-Holder, and H. Keller, Evidence for strong lattice effects as revealed from huge unconventional oxygen isotope effects on the pseudogap temperature in $La_{2-x}Sr_xCuO_4$, Phys. Rev. B **95**, 014514 (2017).

[34] J. Tranquada, B. Sternlieb, J. Axe, Y. Nakamura, and S. Uchida, Evidence for stripe correlations of spins and holes in copper oxide superconductors, Nature (London) **375**, 561 (1995).

[35] G. Ghiringhelli, M. Le Tacon, M. Minola, S. Blanco-Canosa, C. Mazzoli, N. B. Brookes, G. M. De Luca, A. Frano, D. G. Hawthorn, F. He, T. Loew, M. M. Sala, D. C. Peets, M. Salluzzo, E. Schierle, R. Sutarto, G. A. Sawatzky, E. Weschke, B. Keimer, and L. Braicovich, Long-range incommensurate charge fluctuations in (Y, Nd) $Ba_2Cu_3O_{6+x}$, Science **337**, 821 (2012).

[36] J. Chang, E. Blackburn, A. T. Holmes, N. B. Christensen, J. Larsen, J. Mesot, R. Liang, D. A. Bonn, W. N. Hardy, A. Watenphul, M. von Zimmermann, E. M. Forgan, and S. M. Hayden, Direct observation of competition between superconductivity and charge density wave order in $YBa_2Cu_3O_y$, Nat. Phys. **8**, 871 (2012).

[37] E. Fradkin, S. A. Kivelson, and J. M. Tranquada, *Colloquium:* Theory of intertwined orders in high temperature superconductors, Rev. Mod. Phys. **87**, 457 (2015).

[38] B. Keimer, S. A. Kivelson, M. R. Norman, S. Uchida, and J. Zaanen, From quantum matter to high-temperature superconductivity in copper oxides, Nature (London) **518**, 179 (2015).

[39] S. A. Kivelson, I. P. Bindloss, E. Fradkin, V. Oganesyan, J. M. Tranquada, A. Kapitulnik, and C. Howald, How to detect fluctuating stripes in the high-temperature superconductors, Rev. Mod. Phys. **75**, 1201 (2003).

[40] Z. Guguchia, *et al.*, Using uniaxial stress to probe the relationship between competing superconducting states in a cuprate with spin-stripe order, Phys. Rev. Lett. **125**, 097005 (2020).

[41] A. Ricci, N. Poccia, G. Campi, S. Mishra, L. Müller, B. Joseph, B. Shi, A. Zozulya, M. Buchholz, C. Trabant, J. C. T. Lee, J. Viefhaus, J. B. Goedkoop, A. A. Nugroho, M. Braden, S. Roy, M. Sprung, and C. Schüssler-Langeheine, Measurement of spin dynamics in a layered nickelate using x-Ray photon correlation spectroscopy: Evidence for intrinsic destabilization of incommensurate stripes at low temperatures, Phys. Rev. Lett. **127**, 057001 (2021).

[42] J. Zhang, Y.-S. Chen, D. Phelan, H. Zheng, M. R. Norman, and J. F. Mitchell, Stacked charge stripes in the quasi-2D trilayer

nickelate $La_4Ni_3O_8$, Proc. Natl. Acad. Sci. USA **113**, 8945 (2016).

[43] J. Zhang, D. M. Pajerowski, A. S. Botana, H. Zheng, L. Harriger, J. Rodriguez-Rivera, J. P. C. Ruff, N. J. Schreiber, B. Wang, Y.-S. Chen, W. C. Chen, M. R. Norman, S. Rosenkranz, J. F. Mitchell, and D. Phelan, Spin stripe order in a square planar trilayer nickelate, Phys. Rev. Lett. **122**, 247201 (2019).

[44] Y. Li, *et al.*, Distinct ultrafast dynamics of bilayer and trilayer nickelate superconductors regarding the density-wave-like transitions, Sci. Bull. **70**, 180 (2025).

[45] D.-H. Gim, C. H. Park, and K. H. Kim, Orbital-selective quasiparticle depletion across the density wave transition in trilayer nickelate $La_4Ni_3O_{10}$, Phys. Rev. Lett. **135**, 136505 (2025).

[46] S. Deswal, D. Kumar, D. Rout, S. Singh, and P. Kumar, Dynamics of electron-electron correlated to electron–phonon coupled phase progression in trilayer nickelate $La_4Ni_3O_{10}$, Appl. Phys. Lett. **127**, 071903 (2025).

[47] A. Suthar, V. Sundaramurthy, M. Bejas, C. Le, P. Puphal, P. Sosa-Lizama, A. Schulz, J. Nuss, M. Isobe, P. A. van Aken, Y. E. Suyolcu, M. Minola, A. P. Schnyder, X. Wu, B. Keimer, G. Khaliullin, A. Greco, and M. Hepting, Multiorbital character of the density wave instability in $La_4Ni_3O_{10}$, arXiv:2508.06440.

[48] Cambridge Crystallographic Data Centre (CCDC) Deposition Number is 2485140.

[49] See Supplemental Material at http://link.aps.org/supplemental/10.1103/nrqn-m22c for additional information on the μSR, neutron powder diffraction, and magnetic susceptibility experiments, which also includes Refs. [85,86].

[50] A. Amato and E. Morenzoni, *Introduction to Muon Spin Spectroscopy. Applications to Solid State and Material Sciences* (Springer, Cham, Switzerland, 2024).

[51] A. Yaouanc and P. D. de Réotier, *Muon Spin Rotation, Relaxation, and Resonance* (Oxford Science Publications, New York, 2011).

[52] *Muon Spectroscopy. An Introduction,* edited by S. J. Blundell, R. De Renzi, T. Lancaster, and F. L. Pratt (Oxford University Press, Oxford, 2022).

[53] A. W. Overhauser, Mechanism of antiferromagnetism in dilute alloys, J. Phys. Chem. Solids **13**, 71 (1960).

[54] A. Schenck, D. Andreica, F. N. Gygax, and H. R. Ott, Extreme quantum behavior of positive muons in $CeAl_2$ below 1 K, Phys. Rev. B **65**, 024444 (2001).

[55] A. Amato, P. Dalmas de Réotier, D. Andreica, A. Yaouanc, A. Suter, G. Lapertot, I. M. Pop, E. Morenzoni, P. Bonfà, F. Bernardini, and R. De Renzi, Understanding the μSR spectra of MnSi without magnetic polarons, Phys. Rev. B **89**, 184425 (2014).

[56] R. Khasanov, A. Amato, P. Bonfà, Z. Guguchia, H. Luetkens, E. Morenzoni, R. De Renzi, and N. D. Zhigadlo, High-pressure magnetic state of MnP probed by means of muon-spin rotation, Phys. Rev. B **93**, 180509(R) (2016).

[57] H. Boller and A. Kallel, First order crystallographic and magnetic phase transition in CrAs, Solid State Commun. **9**, 1699 (1971).

[58] R. Khasanov, Z. Guguchia, I. Eremin, H. Luetkens, A. Amato, P. K. Biswas, C. Rüegg, M. A. Susner, A. S. Sefat, N. D. Zhigadlo, and E. Morenzoni, Pressure-induced electronic phase separation of magnetism and superconductivity in CrAs, Sci. Rep. **5**, 13788 (2015).

[59] R. Fernandes, A. Chubukov, and J. Schmalian, What drives nematic order in iron-based superconductors? Nat. Phys. **10**, 97 (2014).

[60] H. LaBollita, J. Kapeghian, M. R. Norman, and A. S. Botana, Electronic structure and magnetic tendencies of trilayer $La_4Ni_2O_{10}$ under pressure: Structural transition, molecular orbitals, and layer differentiation, Phys. Rev. B **109**, 195151 (2024).

[61] R. Khasanov, Z. Guguchia, A. Maisuradze, D. Andreica, M. Elender, A. Raselli, Z. Shermadini, T. Goko, F. Knecht, E. Morenzoni, and A. Amato, High pressure research using muons at the Paul Scherrer Institute, High Pressure Res. **36**, 140 (2016).

[62] M. Cardona and M. L. W. Thewalt, Isotope effects on the optical spectra of semiconductors, Rev. Mod. Phys. **77**, 1173 (2005).

[63] J. Menéndez, J. B. Page, and S. Guha, The isotope effect on the Raman spectrum of molecular C_{60}, Philos. Mag. B **70**, 651 (1994).

[64] J. M. Zhang, T. Ruf, M. Cardona, O. Ambacher, M. Stutzmann, J.-M. Wagner, and F. Bechstedt, Raman spectra of isotopic GaN, Phys. Rev. B **56**, 14399 (1997).

[65] A. Amato, H. Luetkens, K. Sedlak, A. Stoykov, R. Scheuermann, M. Elender, A. Raselli, and D. Graf, The new versatile general purpose surface-muon instrument (GPS) based on silicon photomultipliers for μSR measurements on a continuous-wave beam, Rev. Sci. Instrum. **88**, 093301 (2017).

[66] Y. Meng, Y. Yang, H. Sun, S. Zhang, J. Luo, L. Chen, X. Ma, M. Wang, F. Hong, X. Wang, and X. Yu, Density-wave-like gap evolution in $La_3Ni_2O_7$ under high pressure revealed by ultrafast optical spectroscopy, Nat. Commun. **15**, 10408 (2024).

[67] Y. Cao, A. Liu, B. Wang, M. Zhang, Y. Qi, T. J. Hicken, H. Luetkens, Z. Fu, J. S. Gardner, J. Zhao, and H. Guo, Complex spin-density-wave ordering in $La_4Ni_3O_{10}$, Phys. Rev. B **112**, 174423 (2025).

[68] K. Conder, Material aspects of oxygen isotope effect studies in high-temperature superconductors, Physica C **614**, 1354376 (2023).

[69] K. Conder, Oxygen diffusion in the superconductors of the YBaCuO family: isotope exchange measurements and models, Mater. Sci. Eng.: R: Rep. **32**, 41 (2001).

[70] P. Atkins, J. de Paula, and J. Keeler, *Physical Chemistry* (Oxford University Press, Oxford).

[71] R. Khasanov, Perspective on muon-spin rotation/relaxation under hydrostatic pressure, J. Appl. Phys. **132**, 190903 (2022).

[72] A. Suter and B. Wojek, Musrfit: A free platform-independent framework for μSR data analysis, Phys. Procedia **30**, 69 (2012).

[73] A. Schenck, *Muon Spin Rotation Spectroscopy: Principles and Applications in Solid State Physics* (Adam Hilger, Bristol, 1985).

[74] S. J. Blundell and T. Lancaster, DFT + μ: Density functional theory for muon site determination, Appl. Phys. Rev. **10**, 021316 (2023).

[75] B. Huddart, A. Hernandez-Melian, T. Hicken, M. Gomilsek, Z. Hawkhead, S. Clark, F. Pratt, and T. Lancaster, MuFinder: A program to determine and muon stopping sites, Comput. Phys. Commun. **280**, 108488 (2022).

[76] S. J. Clark, M. D. Segall, C. J. Pickard, P. J. Hasnip, M. I. Probert, K. Refson, and M. C. Payne, First principles methods using CASTEP, Z. Kristallogr.—Cryst. Mater. **220**, 567 (2005).

[77] J. P. Perdew, A. Ruzsinszky, G. I. Csonka, O. A. Vydrov, G. E. Scuseria, L. A. Constantin, X. Zhou, and K. Burke, Restoring the density-gradient expansion for exchange in solids and surfaces, Phys. Rev. Lett. **100**, 136406 (2008).

[78] H. J. Monkhurst and J. D. Pack, Special points for Brillouin-zone integrations, Phys. Rev. B **13**, 5188 (1976).

[79] P. Bonfà, I. J. Onuorah, and R. De Renzi, Introduction and a quick look at MUESR, the magnetic structure and muon embedding site refinement suite, JPS Conf. Proc. **21**, 011052 (2018).

[80] https://almax-easylab.com/product/easylab-pcell-15-30/.

[81] P. Fischer, G. Frey, M. Koch, M. Könnecke, V. Pomjakushin, J. Schefer, R. Thut, N. Schlumpf, R. Bürge, U. Greuter, S. Bondt, and E. Berruyer, High-resolution powder diffractometer HRPT for thermal neutrons at SINQ, Physica B **276–278**, 146 (2000).

[82] J. Schefer, P. Fischer, H. Heer, A. Isacson, M. Koch, and R. Thut, A versatile double-axis multicounter neutron powder diffractometer, Nucl. Instrum. Methods Phys. Res. Sect. A **288**, 477 (1990).

[83] V. Petříček, L. Palatinus, J. Plášil, and M. Dušek, Jana2020—A new version of the crystallographic computing system Jana, Z. Kristallogr. **238**, 271 (2023).

[84] J. Rodríguez-Carvajal, Recent advances in magnetic structure determination by neutron powder diffraction Author links open overlay panel, Physica B **192**, 55 (1993).

[85] P. Scherrer, Bestimmung der inneren Struktur und der Größe von Kolloidteilchen mittels Röntgenstrahlen, in *Kolloidchemie Ein Lehrbuch*, Chemische Technologie in Einzeldarstellungen (Springer, Berlin, Heidelberg, 1912).

[86] J. Langmann, H. Kepenci, G. Eickerling, K. Batke, A. Jesche, M. Xu, P. Canfield, and W. Scherer, Experimental x-ray charge-density studies—A suitable probe for superconductivity? A case study on MgB_2, J. Phys. Chem. A **126**, 8494 (2022).